

How far poleward can the seasonal precipitation maxima over land extend under high obliquity?

Jing Han¹ · Larissa E. Back² · Zhengyu Liu³ · Xinyu Wen¹

Received: 14 June 2019 / Accepted: 30 March 2020 © Springer-Verlag GmbH Germany, part of Springer Nature 2020

Abstract

The seasonal response of the poleward extent of continental precipitation maxima to high obliquity and its controlling mechanisms are examined using the NCAR-CESM and Budyko-Sellers energy balance model. In CESM, the latitude of the poleward-most continental precipitation maximum (denoted as ϕ_{mp}) migrates poleward with increased obliquity, but is limited to equatorward of the latitude of maximum daily insolation. Some insight is gained on the controlling mechanism of the migration of ϕ_{mp} in the Budyko-Sellers model, assuming ϕ_{mp} coinciding with the position of maximum surface moist static energy (denoted as Θ_{mp}) as in the present-day observation and CESM pre-industrial simulation. Heat capacity exerts a primary control on ϕ_{mp} such that ϕ_{mp} is determined by the position of maxima of accumulated insolation over the radiative relaxation time and therefore lies equatorward of the maximum daily insolation. Variations of surface albedo and horizontal heat transport, as secondary effects, further shift the ϕ_{mp} . This understanding from the Budyko-Sellers model, however, fails in CESM in the case of high obliquity of 40°, with ϕ_{mp} now lying equatorward of Θ_{mp} . This separation between ϕ_{mp} and Θ_{mp} is explained by the constraint of rotation on the latitudinal range of weak temperature gradients, which is the prerequisite for the prediction of ϕ_{mp} from Θ_{mp} . When the rotation rate is reduced, the latitudinal range of weak temperature gradients expands poleward roughly following the change of the equatorial Rossby radius, allowing ϕ_{mp} moving close to Θ_{mp} .

 $\textbf{Keywords} \ \ Seasonal \ land \ precipitation \cdot Poleward \ migration \cdot High \ obliquity \cdot Surface \ moist \ static \ energy \cdot CGCM \cdot Diffusive \ energy \ balance \ model$

1 Introduction

The seasonal north–south migration of the intertropical convergence zone (ITCZ) is accompanied by monsoon onset and meridional migration of the monsoon system (Charney 1969b; Wang 1994, 2009; Chao and Chen 2001; Wang and Ding 2008; Wang et al. 2014). When using the tropical precipitation maximum along each longitude to characterize the

- ☐ Jing Han hanj@pku.edu.cn
- ☑ Zhengyu Liu liu.7022@osu.edu

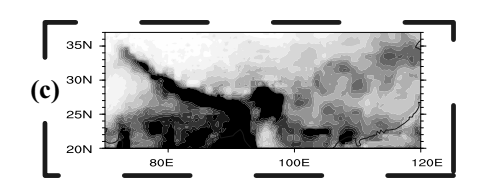
Published online: 10 April 2020

- Laboratory for Climate and Ocean-Atmosphere Studies, Department of Atmospheric and Oceanic Sciences, School of Physics, Peking University, Beijing 100871, People's Republic of China
- ² University of Wisconsin-Madison, Madison, WI, USA
- The Ohio State University, 154 N. Oval Mall, Columbus, OH 43210, USA

position of ITCZ, the ITCZ over land approximately coincides with the location of the continental monsoon rainfall maxima¹ (Wang 2009; An et al. 2015), migrating seasonally over thousands of kilometers, into the Northern Hemisphere in boreal summer and back to the Southern Hemisphere in boreal winter (Fig. 1a). Previous research on the seasonal migration of monsoon rainfall mainly relied on the studies of the ITCZ's migration (Riehl 1979; Philander et al. 1996; Stager et al. 2011). However, both the continental monsoon precipitation maxima and the ITCZ have significant zonal heterogeneity. The ITCZ over land can well describe the migration of the tropical monsoons (Wang 2009; Wang et al. 2014) rather than the subtropical monsoons. For example, in the East Asian monsoon, North American monsoon and

¹ The latitude of continental monsoon rainfall maximum, different from the ITCZ's definition, is defined as the location of maximum precipitation within the monsoonal fraction on each longitude. Monsoon regions are defined as the regions where (a) the local summerminus-winter precipitation rate exceeds 2 mm day⁻¹ and (b) the local summer precipitation exceeds 55% of the annual total, as in Wang and Ding (2008).





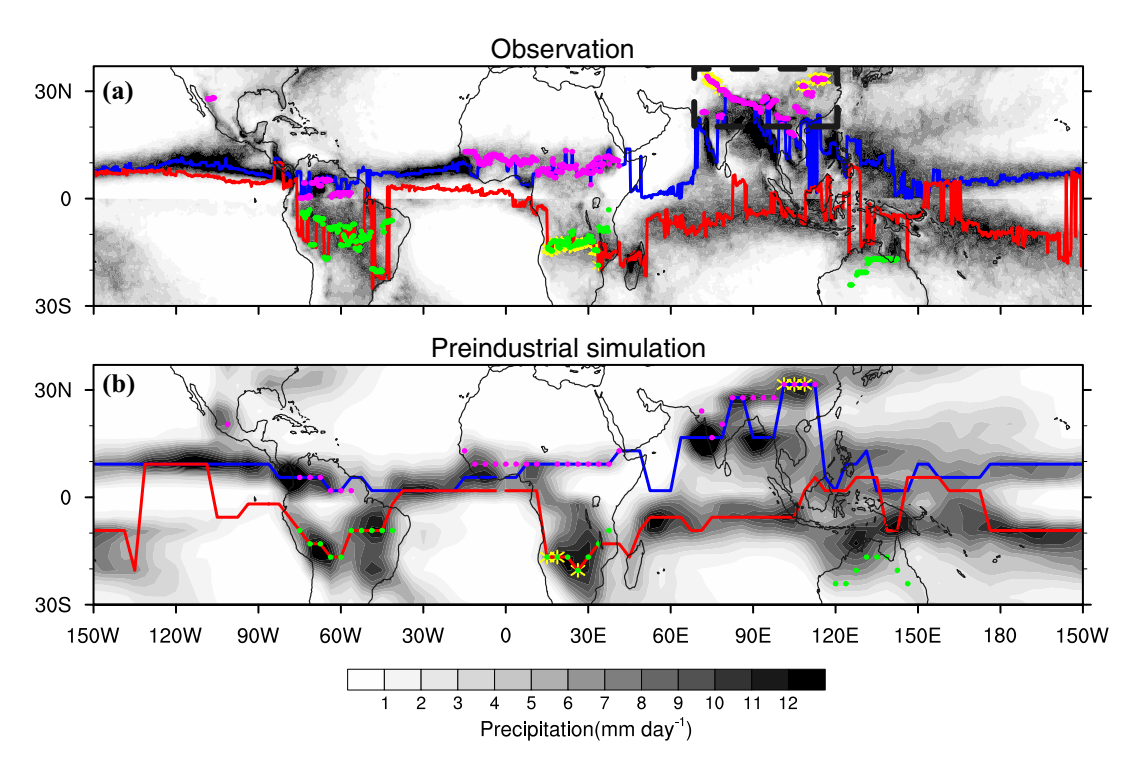


Fig. 1 Spatial distributions of precipitation (shade, mm/day) spliced by boreal summer ($0 \sim 90 \text{ N}$ in July) and austral summer ($0 \sim 90 \text{ S}$ in January), for (a) the observation and (b) our CESM pre-industrial experiment. Blue (red) lines show zonally varying ITCZ in July (January); magenta (green) dots show the positions of continental monsoon precipitation maxima in July (January). Yellow asterisks in a show the 40 poleward-most points among the magenta (green)

dots in July (January). Yellow asterisks in **b** show the 3 poleward-most points among the magenta (green) dots in July (January). Diagram **c** zooms in the area within the dashed box in **a** for presenting the rainfall pattern clearly. The observational precipitation is from the Tropical Rainfall Measuring Mission (TRMM) 3B42 dataset $(0.25^{\circ} \times 0.25^{\circ}$, Huffman et al. 2007) for 1998–2007

Australian monsoon, the continental monsoon rainfall maxima are the secondary precipitation maxima on the same longitudes, with the maximum precipitation falling over the ocean near the equator. Namely, the continental monsoon rainfall maxima in these subtropical regions are located at the poleward of the ITCZ at the same longitudes. Thus, using the ITCZ as an indicator actually underestimates the seasonal migration range of the land monsoon precipitation maxima. It deserves further exploration that how to more accurately measure the seasonal migration of the continental monsoon precipitation maxima.

The seasonal migrations of the ITCZ and the global monsoonal rainfall maxima are significantly correlated with the seasonal variation of solar radiative forcing (e.g., Webster and Fasullo 2003; Broccoli et al. 2006; Trenberth et al. 2006). Changing the Earth's orbital parameters (obliquity,

perihelion, and eccentricity) will cause the seasonal and latitudinal distribution of the solar radiation received by the earth to change, and then will result in changes in the seasonal migration of the continental monsoon precipitation maxima (e.g., Tuenter et al. 2003; Schneider et al. 2014; Bosmans et al. 2015; Wu et al. 2016; Bischoff et al. 2017). Among the three orbital elements, it is the obliquity that contributes most significantly to the seasonal cycle and meridional contrast of solar insolation. Besides, varying obliquity does not change the total annual top-ofatmosphere insolation on the Earth. The obliquity varies between 22.1° to 24.5° (currently 23.5°) over a period of about 41,000 years (Milankovitch 1941). Paleoclimate studies show that the continental monsoon precipitation extends poleward as the obliquity is increased (e.g. from 22.28° to 24.2°, Wu et al. 2016). However, the extension is limited



within the band of 30° S-30° N. An interesting question is therefore, if the obliquity is increased dramatically, can the continental summer monsoon precipitation extend poleward freely? If not, how far poleward can the continental summer monsoon precipitation maxima reach quantitatively? What mechanisms limit the continental summer monsoon precipitation maxima to extend poleward? These questions have not been well answered. Most studies on the climate forced by high obliquity have been done in the context of both paleoclimates (e.g. Oglesby and Ogg 1998; Jenkins 2000) and habitability of exoplanets (e.g. Williams and Pollard 2003; Ferreira et al. 2014; Armstrong et al. 2014; Linsenmeier et al. 2015; Wang et al. 2016; Nowajewski et al. 2018; Kang 2019a, b). There have been a few studies on the dynamics of the atmospheric circulation at high obliquity (e.g. Ferreira et al. 2014; Guendelman and Kaspi 2018; Kang et al. 2019). However, few studies have explored the mechanisms of the extremely poleward shift of continental monsoon rainfall maximum at high obliquity. Studying this question can help us improve our understanding of monsoon dynamics.

In this paper, we are mostly interested in the extreme latitudinal shift of the continental monsoon precipitation maximum. This is best represented by the latitude of the poleward-most maximum monsoonal precipitation (denotedas ϕ_{mn}) among those summer continental monsoon precipitation maxima (magenta/green dots in Fig. 1a). This metric ϕ_{mp} may be viewed as a relatively pure continental response that is subject to less ocean influence. Since the monsoonal precipitation has a relatively large seasonal migration over the Africa-Europe-Asia continent (within the regions of 15 W-120 E) which has a broad land coverage both latitudinally and longitudinally, we will hereafter determine the ϕ_{mn} from the rainfall in this region. To capture the (longitudinally) large scale monsoonal frontal structure, we define ϕ_{mn} as the weighted mean position of the group of the most poleward land precipitation maxima points.² In the highresolution $(0.25^{\circ} \times 0.25^{\circ})$ observation, ϕ_{mp} in each month in local summers (asterisks in Fig. 2a1) will be calculated as the mean position of the 40 poleward-most points (φ_n , n = 1, 2, 3, ..., 40) among the continental monsoon precipitation maxima within 15 W-120E, weighted by their corresponding area-weighted continental precipitation P_n :

$$\phi_{mp} = \frac{\sum_{n=1}^{n=40} \varphi_n P_n \cos(\varphi_n)}{\sum_{n=1}^{n=40} P_n \cos(\varphi_n)}$$
(1)

For example, the ϕ_{mp} in July is obtained by the weighted mean of the latitudes of the 40 yellow asterisks in Fig. 1a (0–90 N). In our CGCM, the spatial resolution is $3.75^{\circ} \times 3.75^{\circ}$ and therefore the ϕ_{mp} in each month in local summers (asterisks in Fig. 2a2) is obtained as the weighted mean position of the 3 poleward-most points among the continental monsoonal precipitation maxima within 15 W–120 E. As will be discussed in Sect. 5, our major conclusion is robust regardless of the detailed definition of the poleward-most points here.

The seasonal migration of the continental monsoon precipitation maximum will be studied in comparison with the seasonal shift of the precipitation maximum over ocean. The meridional shift of the marine precipitation maximum is generally small (Fig. 1a), owing largely to the ocean's large thermal inertia (e.g. Bordoni and Schneider 2008). Furthermore, over the eastern Pacific and the Atlantic where the equatorial cold tongues exist, the marine precipitation maxima stay north of the equator, due to the combined effort of land-sea distribution (Philander et al. 1996), ocean-atmosphere interactions (Xie and Philander 1994), local orography, notably the Andes (Takahashi and Battisti 2007) and the Atlantic Meridional Overturning Circulation (Marshall et al. 2013). The marine precipitation maxima over the Indian ocean and western Pacific is exceptional in that its migration is comparable with the continental monsoon regions and has also been considered as part of the global monsoon system (Wang and Ding 2008; Wang et al. 2014). Even so, the rainfall distribution over ocean still has largely zonal homogeneity. Hereafter, we will use the latitude of maximum precipitation zonally averaged over ocean, denoted as " ϕ_{ocn} ", as the metric to check the seasonal migration of marine precipitation maximum (solid black line in Fig. 2b1).

Thermodynamically, we generally expect the occurrence of the tropical convection and then precipitation are correlated with some measures related to the column moist stability, such as convective available potential energy (CAPE). As long as the free tropospheric lapse rate doesn't vary much, CAPE is approximately proportional to the difference between surface moist static energy (MSE) and upperlevel saturated MSE (Bohren and Albrecht pp. 297; Back and Bretherton 2009). Due to the large equatorial Rossby radius, free tropospheric meridional temperature gradients in the tropics are small (Charney 1963, 1969a; Held and Hou 1980; Bretherton and Smolarkiewicz 1989; Sobel et al. 2001). Thus, in the tropics, the surface MSE alone roughly determines where the strongest deep conditional instability



This metric is insensitive to the dataset's resolution in boreal summer as confirmed by the comparison of the three precipitation datasets: Tropical Rainfall Measuring Mission (TRMM) 3B42 ($0.25^{\circ} \times 0.25^{\circ}$), Global Precipitation Climatology Project (GPCP) ($2.5^{\circ} \times 2.5^{\circ}$) and CESM ($3.75^{\circ} \times 3.75^{\circ}$). One caveat: in the boreal winter, the CESM exhibits an overestimation compared with TRMM and GPCP. (Not shown).

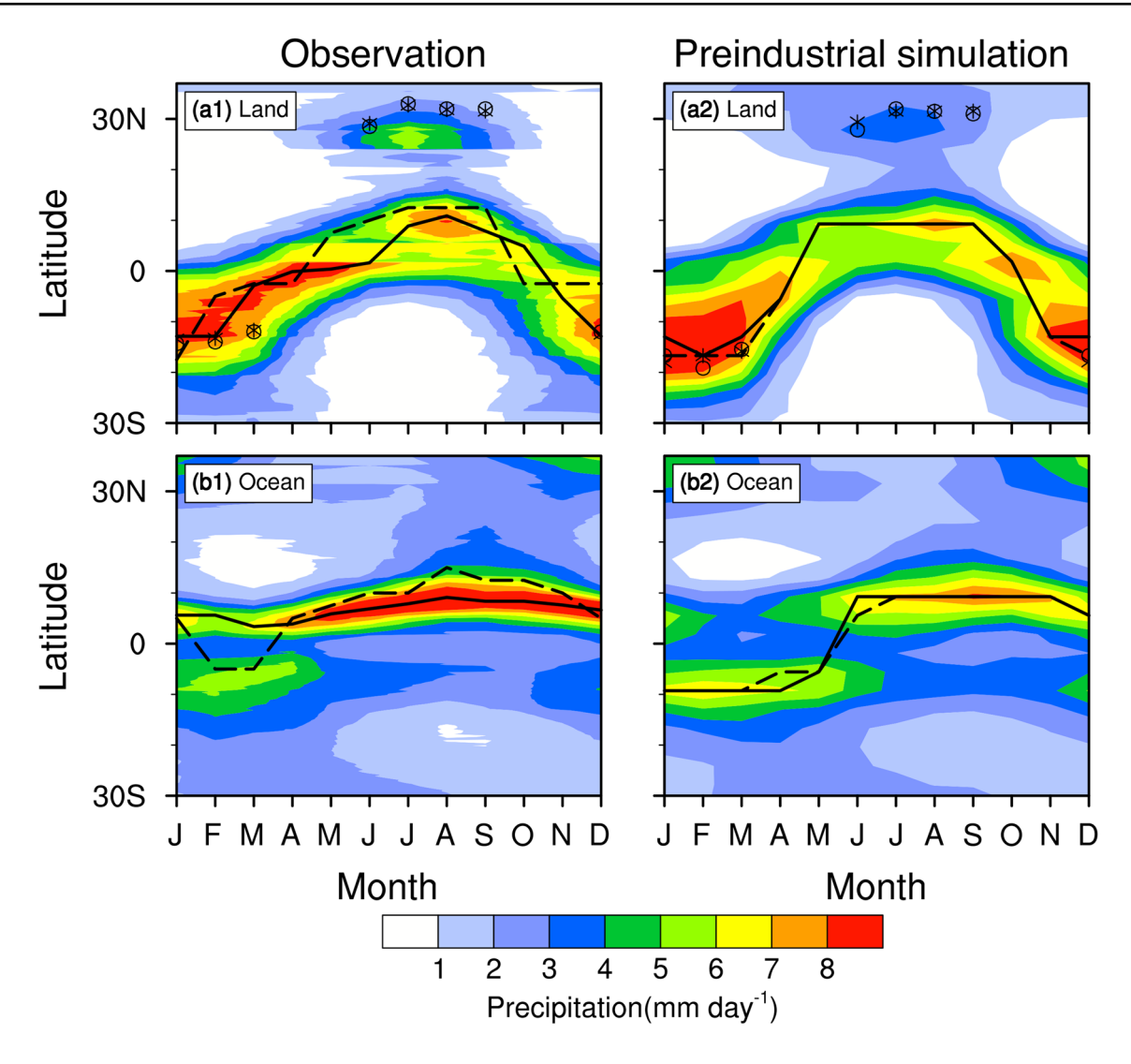


Fig. 2 Seasonal cycle of precipitation (shade, mm/day), the position of maximum mean precipitation (solid black lines), and the position of maximum mean surface moist static energy (dashed lines), for the TRMM observation (left column) and CESM pre-industrial simulation (right column). In **a1** and **a2**, black asterisks (circles) show the ϕ_{mp} (Θ_{mp}) in boreal summer and winter. In **b1** and **b2**, solid (dashed)

lines show the seasonal cycle of the ϕ_{ocn} (Θ_{ocn}). The data for calculating moist static energy is from the NCEP/NCAR reanalysis monthly data for 1998–2007. "Land", "Ocean", and "Land+Ocean", indicate the mean precipitation zonally averaged "over only land", "over only ocean", and "over land and ocean together", respectively

hold, that does not have to be the case. For example, Faulk

et al. (2017) find that the summertime maximum precipita-

tion stays within the tropics and falls far behind the maxi-

mum surface MSE which is located at the summer pole in

an eternal-solstice aquaplanet simulation. However, we use

reasoning about processes that affect the maximum surface MSE as a starting point for reasoning about the maximum

occurs (Nie et al. 2010). In the present-day observation (Fig. 2a1, b1), the latitudes of most poleward precipitation maxima ϕ_{mp} and ϕ_{ocn} coincide with the latitudes of their corresponding maximum surface MSE, denoted as Θ_{mp}^{3} and Θ_{ocn}^{4} respectively. Further away from the equator, where meridional weak temperature gradients (WTG) does not

 3 Θ_{mp} is got as the mean position of the three surface MSE maxima at the corresponding longitudes of the three poleward-most precipitation maxima in our CGCM.

precipitation and examine an energy balance model to get some qualitative pictures of the responses of Θ_{mp} (Θ_{ocn}) and thereby ϕ_{mp} (ϕ_{ocn}) to radiative variations associated with obliquity changes. Then, we will move to a coupled-GCM, relaxing the assumption of coincident maximum surface MSE and maximum precipitation and further exploring the



⁴ Θ_{ocn} is obtained as the latitude of maximum surface MSE zonally averaged over the sections covered by ocean, analogously to the definition of ϕ_{ocn} .

mechanism of the precipitation maxima's seasonal shift. Here, an interesting question is, for an increased obliquity, can the maximum precipitation ϕ_{mp} (ϕ_{ocn}) always catch up with the latitudes of the corresponding maximum surface MSE Θ_{mn} (Θ_{ocn}) in a coupled-GCM? We speculate that ϕ_{mn} (ϕ_{ocn}) cannot follow the $\Theta_{mp}(\Theta_{ocn})$ under an extremely high obliquity. One possible reason is the dynamic constraint of the planetary rotation, which limits the equatorial Rossby radius and in turn the scale on which atmospheric wave processes adjust the environment to form WTG. When Θ_{mn} (Θ_{ocn}) shifts further away from the equator with increasing obliquity and beyond the equatorial Rossby radius, the WTG approximation might still be limited within the equatorial Rossby radius such that ϕ_{mp} (ϕ_{ocn}) is unable to follow Θ_{mp} (Θ_{ocn}). Faulk et al. (2017) attribute the constraint of the mean ITCZ's location away from the maximum surface MSE when WTG no longer applies to a critical curvature (Emanuel 1995), which predicts the presence or absence of a circulation. When the curvature of low-level MSE exceeds a critical value, a circulation is necessary equatorward of this criticality condition. However, this argument is meant to give an upper bound to the locations of the ascending branch of the Hadley circulation and thereby, the ITCZ. It cannot exactly predict where the ITCZ or even ϕ_{mp} is.

It should be noted that the mechanisms controlling the poleward-most latitude of continental precipitation maximum ϕ_{mn} may be different from that of the zonal mean ITCZ and therefore may not be explained simply from the crossequatorial energy flux perspectives. For the zonal mean ITCZ, model simulations suggest that the ITCZ's position can be affected by perturbing the atmospheric energy balance in the extratropics (Manabe and Stouffer 1980; Lea et al. 2003; Chiang and Bitz 2005; Broccoli et al. 2006; Kang et al. 2008, 2009; Yoshimori and Broccoli 2008; Frierson and Hwang 2012, 2013; Donohoe et al. 2013; McGee et al. 2014; Schneider et al. 2014; Bischoff and Schneider 2014, 2016; Adam et al. 2016a, b; Bischoff et al. 2017). An energetic framework has been established that the ITCZ's shift is strongly anti-correlated with the changes of crossequatorial atmospheric energy transport (AET_{EO}). Based on this argument, Bischoff et al. (2017) further develop a conceptual model for the estimation and interpretation of the rainfall response directly to orbital forcing, where the AET_{EO} is assumed to be proportional to the hemispherically averaged insolation difference. Furthermore, the ITCZ is also found to lie near the energy flux equator (EFE), where the column-integrated atmospheric meridional energy fluxes diverge and vanish (Kang et al. 2008). These simple energy flux diagnostics, however, may not apply to the most poleward latitude of maximum land precipitation ϕ_{mn} for, at least, two reasons. First, ϕ_{mp} can be highly localized in longitude extent, and therefore can deviate significantly from the zonal mean (e.g. Fig. 1a, b). Second, the land precipitation at ϕ_{mn}

is sometimes smaller than the marine precipitation maxima at the same longitude (e.g. in the region of East Asian summer monsoon in Fig. 1a, b). For completeness, however, some aspects of the ITCZ's shift with varying obliquity will be discussed from the energetic framework in Appendix B.

Our working strategy is the following. Section 2 introduces the models and simulations. Then, we first check the seasonal migration of the continental maximum precipitation ϕ_{mp} in the CGCM simulations under different obliquities in Sect. 3, with the focus on the cases of high obliquity. To gain insight into the CGCM results, we first study the response in a simple energy balance model and then return to the CGCM. Section 4a uses an energy balance model to explore the controls on the ϕ_{mp} 's poleward migration ideally, based on the assumption of coincidental latitudes of maximum precipitation ϕ_{mp} and maximum surface MSE Θ_{mp} . We will then further study the mechanisms of the ϕ_{mp} 's response in our CGCM in Sect. 4b, with the focus on the effect of different rotation rates. In Sect. 5, we summarize our results and have some further discussions on some related issues.

2 Simulation design

2.1 The complicated model: CESM_{SOM}

To explore the extreme latitudinal shift of the continental maximum precipitation ϕ_{mn} to high obliquity, we employ the coupled Community Earth System Model (CESM1.0, NCAR), which consists of five components and a coupler: CAM4, CLM4, SOM, CICE4, CISM and CPL7 (https:// journals.ametsoc.org/topic/ccsm4-cesm1). For simplicity, the ocean component here is a slab ocean model (SOM) in which the divergence of ocean heat transport is prescribed through a so-called "Q-flux" (Hansen et al. 1988). We estimate the seasonal Q-flux and ocean mixed layer depth from a 2000-year pre-industrial simulation of the CESM1.0 with the full ocean. With the prescribed Q-flux, SST is determined by the energy balance between latent heat, sensible heat, surface radiative flux, and Q-flux. We apply the grid scheme T31_gx3v7 in all the CGCM experiments of this paper. The SOM uses the grid scheme gx3v7, with a uniform 3.6° spacing in the zonal direction and a non-uniform spacing (0.6° near the equator, extending to the maximum 3.4° poleward of 35°N/S and then shrinking gradually to the poles) in the meridional direction. Both the CAM4 and CLM4 use the horizontal spectral grids of 48 × 96 (~3.75°×3.75°), with 26 atmospheric vertical levels. The CICE4 is set to have the same grid as SOM does. This version model is referred to as $\mathsf{CESM}_\mathsf{SOM}$ hereafter.

The CESM_{SOM} pre-industrial simulation (Figs. 1b, 2a2 and b2) largely captures the main features of the precipitation and performs reasonably well in simulating the ϕ_{mn}



and ϕ_{ocn} in comparison with the observation of the Tropical Rainfall Measuring Mission (TRMM) (Huffman et al. 2007) (Figs. 1a, 2a1 and b1). One thing to note here is that the CESM_{SOM} overestimates the rainfall intensity in the East Asian Summer Monsoon and underestimates the rainfall in South Asian Summer Monsoon. This, however, does not affect the qualitative variation of the latitude ϕ_{mp} in boreal summer with increasing obliquity. In addition, the model overestimation of precipitation over the equatorial central Pacific Ocean in boreal winter implies some caveats on the seasonal migration of ϕ_{ocn} , which strengthens the seasonality of ϕ_{ocn} compared with the observations. Nevertheless, CESM_{SOM}, even at such low resolution, can provide a reasonably realistic model for the simulation of the ϕ_{mp} 's and ϕ_{ocn} 's response to obliquity.

Different from the above pre-industrial simulation with realistic topography, for lowering the complexity of exploring the ϕ_{mp} 's response to high obliquity, the CESM_{SOM} simulations discussed below are conducted with flat topography, unless "realistic topography" is expressly specified. We remove the orographic features by setting the surface elevation to 10 m over all land areas. Previous studies have shown significant local impact of topography on monsoonal rainfall, especially in the Northern Hemisphere which has more large-scale terrain than the Southern Hemisphere does (e.g. Hahn and Manabe 1975; Liu et al. 2003; Yanai and Wu 2006; Wang et al. 2008; Boos and Kuang 2010; Wu et al. 2012; Chen et al. 2014). Taking the Tibetan Plateau (TP) as an example, the South Asian Summer Monsoon north of 20°N and the East Asian Summer Monsoon are prominently weakened and the zonal-mean precipitation maxima in the Asian Monsoon region shift towards the equator, without than with TP (Wu et al. 2012).

To assess the responses of ϕ_{mp} to high obliquities in the CESM_{SOM}, we perform a set of "Obliquity Experiments" with the obliquities of 10° (Obliq10), 23.5° (Obliq23.5, control value), 32° (Obliq32), and 40° (Obliq40), at the Earth's rotation rate. Seasonal variations of insolation due to obliquity changes present a very clear asymmetrical pattern with respect to the equator. With an increased obliquity, mid- and high- latitudes experience an increase in summer insolation, while the insolation in low latitudes decreases slightly throughout the year (Fig. 3a1, b1, c1, and d1). Increasing obliquity strengthens the seasonal cycle of insolation in both hemispheres and also generates a larger meridional insolation contrast, which may cause a larger poleward extent of the continental monsoon precipitation maxima. We do not set obliquity larger than 40° due to the limitations of model stability and computing resources. The eccentricity and longitude of the perihelion are kept at the default values of 0.016715 and 102.7° at year 1990. All other boundary conditions (e.g., solar constant, greenhouse gas concentrations) are set to the pre-industrial conditions. To further understand the mechanism behind the response of ϕ_{mp} to high obliquity, we conduct a set of "Rotation Experiments" in CESM_{SOM} (Table 1), where, the rotation rate is reduced from twice down to 1/8th of the current Earth's rotation rate (Ω_E), denoted by $2\Omega_E$, Ω_E , Ω_E , 2, 2, 2, 2, 2, and 2, and 2, all parameters other than rotation rate is kept the same as in the "Obliquity Experiments". All the above CESM_{SOM} experiments are performed for 40-year each and the last steady-state 20-year are used for analysis. All experiments are initialized from the 2000-year pre-industrial run which the Q-flux for the SOM is derived from. Table 1 provides a list of the experiments in CESM_{SOM}. For example, "Obliq23.5_ Ω_E " means that the experiment is under the condition of the present-day obliquity 23.5° and the Earth's rotation rate Ω_E .

Changes in Q-flux will change the land-sea thermal contrast, which will further affect the distribution of continental monsoon precipitation. For reducing the complexity of understanding the ϕ_{mp} 's response to high obliquity, we use the same prescribed Q-flux in all the above CGCM experiments as in the pre-industrial simulation. Each of these simulations is repeated by CESM1.0 with the Parallel Ocean Program version 2 (POP2), which includes ocean dynamics, instead of slab ocean model (SOM) as the ocean component. This version of CESM is referred to as the CESM_{POP}. At this time, O-flux will change as the obliquity is increased, allowing us to see how ocean energy transport affects seasonal movements of land monsoon precipitation. The POP2 is set to have the same horizontal grid as SOM but has 60 vertical levels. For CESM_{POP} experiments, each one is initialized from the same 2000-year pre-industrial run and is integrated for 200 years, a sufficient length of time to reach equalibrium for upper ocean down to 1000 m. The trends of the globally averaged sea surface temperature and upper ocean temperature above 1000 m during the last 50 years are ~0.1 °C/100 years. The last 50 years data is used for analyses. We just decrease the rotation rate in the $CESM_{POP}$ to half of the Earth's rotation rate because the CESM_{POP} is more unstable under high obliquity at a slower rotation rate than the CESM_{SOM}.

Finally, for addressing the robustness of our conclusions, we perform additional simulations with a rectangular sealand configuration to repeat our results in the simulations with realistic sea-land distribution (Fig. 3a3). We just show the key result of this set of idealized sea-land simulations in Sect. 5. More details feed into a companion paper (Han et al., 2020).

2.2 The conceptual model: Budyko-Sellers energy balance model

A useful starting point for understanding the seasonal migration of ϕ_{mp} is the Budyko-Sellers energy balance model [Eq. (2)] (Budyko 1969; Sellers 1969), if we assume that



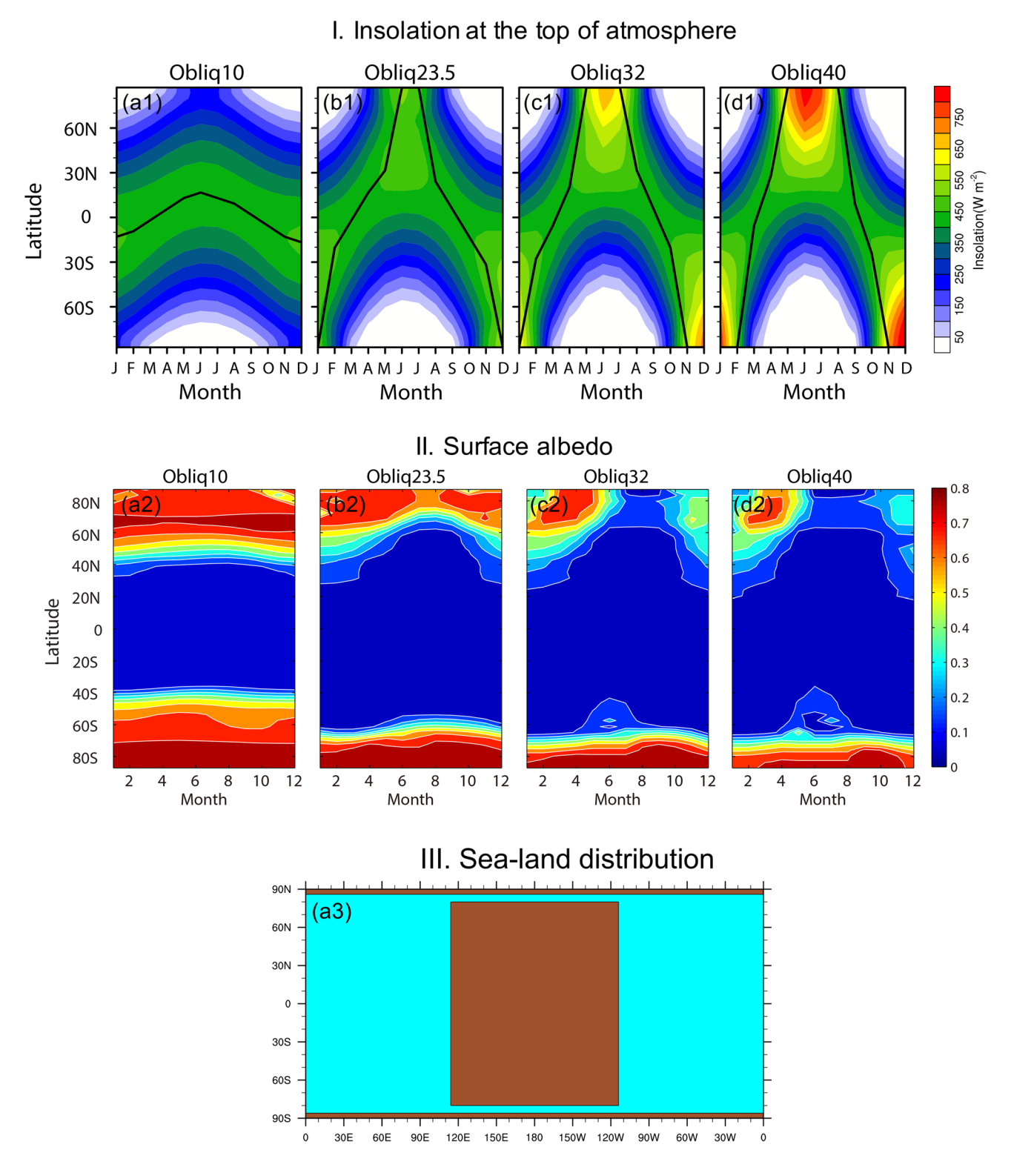


Fig. 3 Model setup. I. Seasonal cycle of insolation (color contours, W m⁻²) at the top of atmosphere, with obliquity increasing from left to right (a1, b1, c1, d1). The black line in each diagram indicates the position of maximum daily insolation. II. Seasonal cycle of surface albedo in the obliquity experiments: Obliq10_ Ω_E (a2), Obliq23.5_ Ω_E

(b2), Obliq32_ Ω_E (c2), Obliq40_ Ω_E (d2), from left to right. III. Sealand distribution in the set of CESM_{SOM} simulations with rectangular land geometry. Brown shade shows the continent; cyan shade shows the ocean



Table 1 Experiments by the CESM

	"Rotation Experiments"				
	$2\Omega_E$	Ω_E	$\Omega_E/2$	$\Omega_E/4$	$\Omega_E/8$
"Obliquity Experiments"		Obliq 10_Ω_E			Obliq $10_\Omega_E/8$
	Obliq23.5_2 Ω_E	Obliq23.5_ Ω_E	Obliq23.5_ Ω_E /2	Obliq23.5_ Ω_E /4	Obliq23.5_ Ω_E /8
		Obliq32 $_\Omega_E$			Obliq32 $_{\it E}$ /8
		Obliq 40_Ω_E			Obliq $40_\Omega_E/8$

the latitude of maximum precipitation ϕ_{mp} always coincides with the latitude of maximum surface MSE Θ_{mp} under various obliquities as the present-day and CESM pre-industrial ϕ_{mp} do (Figs. 2a1 and a2). Thus, we can first learn some basic mechanisms that determine how the location of the maximum surface MSE (Θ_{mp}) , and thus the latitude of maximum precipitation (ϕ_{mp}) , vary qualitatively from an energy balance model perspective.

The EBM is assumed to be zonally homogeneous,

$$C\frac{dT_s(x,t)}{dt} = Q_t(x,t)(1-\alpha) - A - \lambda T_s(x,t) + \frac{d}{dx} \left[D(1-x^2) \frac{dH(x,t)}{dx} \right],$$
(2)

where $x = sin(\varphi)$ and φ is latitude. The parameter C is an effective heat capacity per unit area. The continental and oceanic temperature responses can be simulated individually, to a first order approximation, using different values of heat capacity C (small over land, large over ocean). The e-folding time $\tau = C/\lambda$ describes the system's thermal inertia time scale, where λ is a feedback parameter. Q_t is the insolation at the top of atmosphere (TOA) which is given by our CESM_{SOM} obliquity experiments. The α is surface albedo, $A + \lambda T_s(x, t)$ is the TOA outgoing infrared radiation of surface temperature T_s . The values of A and λ are prescribed as $A = 211.5 \ Wm^{-2}$ and $\lambda = 1.6 \ Wm^{-2}K^{-1}$. These values are obtained by regressing the 20-year monthly zonalmean outgoing longwave radiation versus surface temperature in our control case "Obliq23.5_ Ω_E " ($R^2 = 0.89$). A and λ vary little as changing obliquity. We have verified that this simple model is insensitive to the small changes of A and λ from different obliquities. H is the surface MSE. Based on the formula of surface MSE and the Clausius-Clapeyron equation (Bolton 1980), surface MSE (H) can be approximately calculated as the function of surface temperature (T_s)

$$H = c_{pd}T_s + L_v q_s$$

$$\approx c_{pd}T_s + L_v r_s \frac{R_d}{R_v} \frac{1}{p_s} \left\{ 6.112 hpa * \exp \left[\frac{17.67 * (Ts - 273.15)}{Ts - 29.65} \right] \right\}, \tag{3}$$

where c_{pd} is specific heat of dry air at constant pressure, L_{v} is latent heat of vaporization, r_{s} is surface relative humidity which is assumed to be constant (0.8). R_d is the gas constant of dry air, R_{ν} is the gas constant of water vapor, and p_s is surface pressure. One caveat in the approximate calculation of surface MSE is the constant relative humidity. The term $\frac{d}{dx} \left[D(1-x^2) \frac{dH(x,t)}{dx} \right]$, is a diffusive moist static energy process with the constant diffusivity D to parameterize the meridional heat transport, which is found to perform well by recent studies in some GCMs (Frierson et al. 2007: Hwang and Frierson 2010; Rose et al. 2014; Roe et al. 2015; Liu et al. 2017). We will limit our discussion to the onelayer EBM in spite of its deficiency in simulating the seasonal cycle of the modern climatology (Abbot and Tziperman 2009; Wu Y.-T. 2008). This is because this model can still provide a simple framework to shed some light on our more complex CGCM simulations.

To understand the question: what controls the seasonal migration of the maximum surface MSE Θ_{mp} , and, in turn, ϕ_{mp} , we design three series of idealized simulations (Table 2) to test three possible influential factors: heat capacity, surface albedo, and meridional MSE transport, named as "EBM_local", "EBM_local_a", and "EBM", respectively. Heat capacity determines the magnitude and phase of the system's response to external thermal forcing. Surface albedo varying with latitudes affects the distribution of insolation received on the local surface. Meridional MSE transport acts to redistribute the energy horizontally and thereby probably change the latitudinal position of maximum MSE. These are the reasons why we choose the above possible control factors.

We first perform simulations in the local energy balance model (D=0) to test the effects of heat capacity and surface albedo on the seasonal migration of Θ_{mp} . The effect of meridional MSE transport on Θ_{mp} is then studied by adding the diffusion term with a non-zero D. Specifically, the simulations "EBM_local" are conducted by varying heat capacity C from 0.04×10^7 , 1.0×10^7 , to $4.0 \times 10^7 Jm^{-2}K^{-1}$, corresponding a mixed layer depth of approximately 0.1 m, 2.5 m and 10 m respectively. The albedo α is assumed a value 0.3



Table 2 Idealized simulations by the energy balance model

	"EBM_local"	"EBM_local_a"	"EBM"
	$(D=0, \alpha = 0.3; \text{ varying } C \text{ from } 0.04 \times 10^7, \\ 1.0 \times 10^7, \text{ to } 4.0 \times 10^7 \text{ Jm}^{-2} \text{K}^{-1})$	$(D=0, \alpha \text{ varying latitudinally})$	($\alpha = 0.3$, $C = 4.0 \times 10^7 Jm^{-2}K^{-1}$; varying D from 0.0 , 1.0×10^{-4} , to 5.0×10^{-4} kgm ⁻² s ⁻¹
Obliq10	EBM_local_10	EBM_local_a_10	EBM_10
Obliq23.5	EBM_local_23.5	EBM_local_a_23.5	EBM_23.5
Oblig32	EBM local 32	EBM local a 32	EBM 32
Obliq52		=	- -

The meanings of digits in the idealized simulations' name:

uniformly everywhere and the diffusivity D equals zero. The simulations "EBM_local_a" are similar to the simulations "EBM_local" but incorporate the latitudinal variations of surface albedo. The surface albedo⁵ for each obliquity case of "EBM_local_a" is given by the seasonal cycle of zonal-mean albedo calculated from the individual CESM_{SOM} obliquity experiments above (Fig. 3a2, b2, c2 and d2). The simulations "EBM" adopts a finite diffusivity D > 0, setting a spatially uniform diffusivity D from 0.0 to 1×10^{-4} and, eventually, 5×10^{-4} kg $m^{-2}s^{-1}$ under the condition of heat capacity $C = 4.0 \times 10^7 Jm^{-2}K^{-1}$, while all other parameters remain the same as in "EBM_local". Under the conditions of heat capacity $C = 0.04 \times 10^7$ and $1.0 \times 10^7 Jm^{-2}K^{-1}$, varying diffusivity D brings forth the similar conclusions qualitatively, so they are not shown in this paper.

3 The ϕ_{mp} under high obliquity in the CESM $_{\rm SOM}$

We will first examine the seasonal response of the ϕ_{mp} under various obliquities in a comprehensive CGCM, i.e. the CESM_{SOM}, and explore the relation between the locations of the poleward-most maximum continental precipitation ϕ_{mp} and maximum continental surface MSE Θ_{mp} . For comparison, the responses of the marine ϕ_{ocn} and the Θ_{ocn} to various obliquities will also be discussed.

The seasonal response of ϕ_{mp} to obliquity variation is presented in Fig. 4a1, a2, a3, and a4. Black asterisks show the positions of the ϕ_{mp} in the boreal summer (JJAS) and winter (DJFM). With increasing obliquity from 10° to 40°,

the span of the ϕ_{mp} 's seasonal migration increases gradually from 5 S-10 N to 30 S-35 N. Under obliquity 40°, the ϕ_{mp} has moved to the latitude of the poleward continental boundary in the Southern Hemisphere (except for the Antarctic Continent) in boreal winter. In boreal summer, the ϕ_{mp} coincides with the latitude of its corresponding maximum surface MSE Θ_{mp} (black circles) under the low obliquities (10° and 23.5°) but falls behind the Θ_{mp} under the high obliquities, especially for obliquity 40°. In boreal winter, the ϕ_{mp} always roughly coincides with the Θ_{mp} , presumably associated with the land's finite longitudinal extent. The ϕ_{ocn} varies similarly to ϕ_{mp} but by a smaller amplitude with each increase in obliquity (Fig. 4b1, b2, b3, b4).

Previous work argues that the advection of low moist enthalpy from the ocean, where heat storage opposes summer warming, into the continent, termed as the ventilation effect, is a leading effect that limits the poleward edge (measured by 2 mm/day contour) of the summer monsoonal precipitation (Chou and Neelin 2001, 2003; Neelin 2007). This also holds for our "Obliquity Experiments" of CESM_{SOM} (Fig. 5). The horizontal moist enthalpy advection is calculated as $-\langle v \bullet \nabla E \rangle$, where $\langle \bullet \rangle$ indicates a vertical mass integral [i.e. $\int (\bullet)dp/g$] with (\bullet) representing the temporal mean, v is horizontal wind vector, and $E = c_{pd}T + L_{\nu}q$ is atmospheric moist enthalpy. The horizontal moist enthalpy advection in July (January) is shown in the band 0-90 N (0-90S) of Fig. 5a-d. Comparing the patterns of rainfall (vellow contour lines) and horizontal moist enthalpy advection (color shades), we recognize the effect of ventilation in limiting the overall extent of the continental monsoon rainfall in our all cases of obliquity 10° , 23.5° , 32° , and 40° (Fig. 5a–d). For example, in July, the poleward edge (the 2 mm/day contour) of the continental precipitation over the Asian monsoon always follow the equatorward edge of the higher-latitudinal negative advection shades at different obliquities. The continental precipitation extends poleward following the poleward shift of the strong negative horizontal moist enthalpy advection as increasing obliquity.



[&]quot;EBM" means the model used is a diffusive energy balance model, described by Eq. (2)

[&]quot;local" indicates a simplest version with a local radiative equilibrium (D=0). Otherwise, the model is a diffusive one

[&]quot;a" indicates that the model uses a latitudinally-varied surface albedo. Otherwise, the model uses a uniform surface albedo of 0.3

 $^{^{5}}$ Surface albedo=(FSDS-FSNS)/FSDS, where "FSDS" is downwelling solar flux at surface and "FSNS" is net solar flux at surface. FSDS and FSNS are obtained from our CESM $_{\rm SOM}$ obliquity simulations.

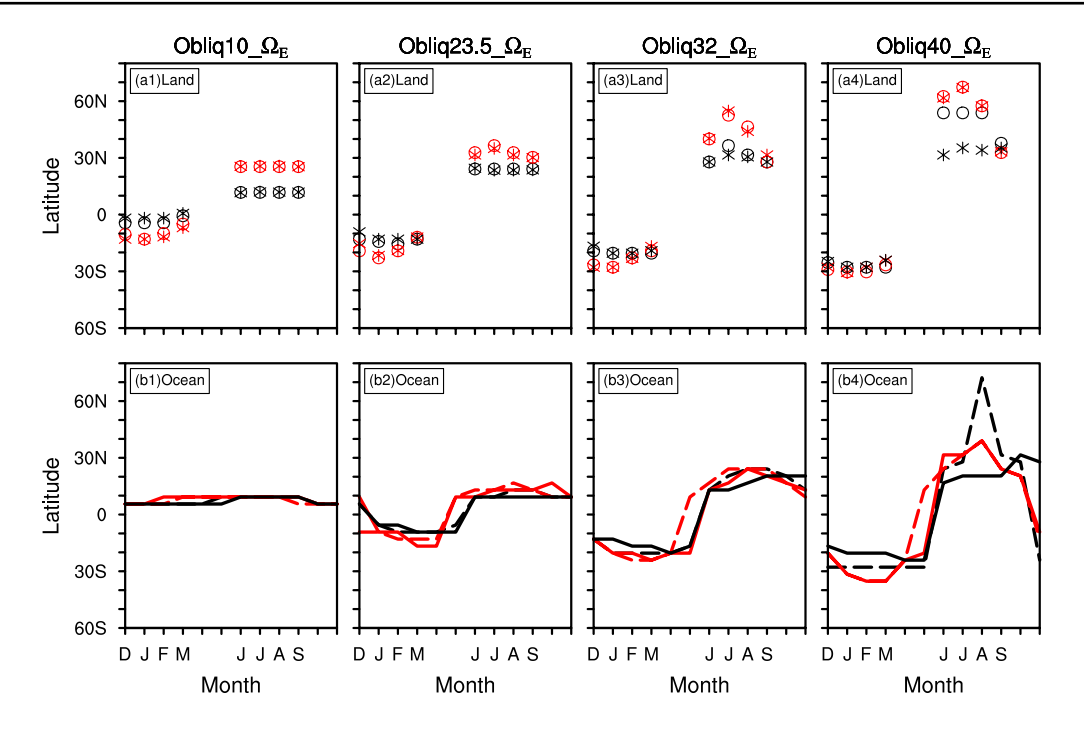


Fig. 4 Seasonal cycle of the ϕ_{mp} (black asterisks, top row) and ϕ_{ocn} (black solid lines, bottom row), for "Obliquity Experiments" at the Earth's rotation rate Ω_E with flat topography. Black circles show the latitude of maximum continental surface MSE Θ_{mp} as similar as in Fig. 2a1 and a2. Black dashed lines show the latitude of maximum

marine surface MSE Θ_{ocn} as similar as in Fig. 2b1 and b2. Red markers/lines have the similar meanings as the black markers/lines but for "Obliquity Experiments" at the rotation rate of $\Omega_E/8$ with flat topography

Those also occurs for local-summer precipitation over North African, North American, South American, and Australian monsoon regions. Since the maxima of monsoonal continent rainfall which we are mostly interested in lie equatorward of its poleward edge, ventilation effect provides an upper bound for the maxima's shifts but can not quantitatively predict the latitude of the maxima, not to mention the ϕ_{mn} [calculated by the three red asterisks each hemisphere as Eq. (1)]. Furthermore, the rainfall maxima over East Asia in Obliq32 $\underline{\Omega}_E$ and over West Africa in Obliq 40_Ω_E are located in the area where positive horizontal moist enthalpy advection exists on site and also at its poleward side, yet, it does not support a further poleward migration of those rainfall maxima and thus ϕ_{mp} (Fig. 5d). That means there must be other mechanisms further constraining the ϕ_{mp} 's poleward shift in addition to the ventilation effect, a topic to be continued in Sect. 4.

4 Interpretation of the response of $\phi_{\it mp}$ to high obliquity

4.1 Insight from the Budyko-Sellers energy balance model

We can get insight into some basic mechanisms that determine how far the latitude of maximum precipitation ϕ_{mp}

extends seasonally from an energy balance model perspective, if we assume that the ϕ_{mp} always coincides with the latitude of maximum surface MSE Θ_{mp} under various obliquities as the present-day and CESM pre-industrial ϕ_{mp} do. We have examined three possible influential factors: heat capacity, surface albedo, and meridional MSE transport in the Budyko-Sellers energy balance model. Then, in the next subsection, we will relax this assumption and further explore the mechanism of the ϕ_{mp} 's seasonal shift in the CESM_{SOM}.

Factor 1: heat capacity

It is obvious that the heat capacity should play a critical role in controlling the seasonal migration of the maximum surface MSE. More specifically, a finite heat capacity tends to limit the poleward extension of the maximum surface MSE, causing a delay in the response relative to the maximum daily insolation forcing (Fig. 5). This can be seen in the simulations "EBM_local" (Table 2, Fig. 6a1, b1, c1, d1). We take the simulation "EMB_local_23.5" as an example (Fig. 6b1). In the limiting case of a very small heat capacity $C = 0.04 \times 10^7 Jm^{-2}K^{-1}$, which corresponds to a relaxation time $\tau \sim 3$ days, the maximum surface MSE (solid blue line) follows the maximum daily insolation (dashed black line) all the way to the pole with no phase shift. When the heat capacity increases,



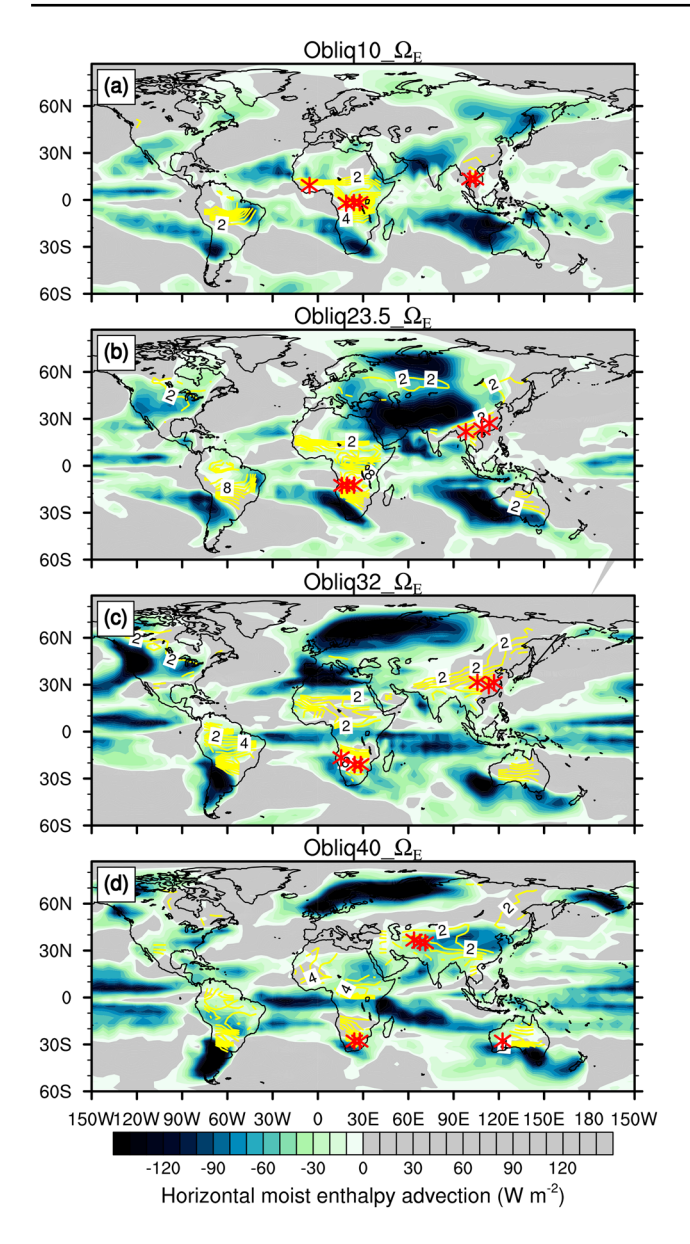


Fig. 5 Spatial distributions of the vertical integral of horizontal moist enthalpy advection $-\langle v \bullet \nabla E \rangle$ (W m⁻², color shade) and land precipitation (mm/day, yellow contours over 2 mm/day; contour interval is 1 mm/day), spliced by boreal summer (0~90 N in July) and austral summer (0~90S in January) for "Obliquity Experiments" at the Earth's rotation rate Ω_E with flat topography (Table 1). Red asterisks in each diagram show the three poleward-most points of the monsoonal precipitation maxima over the longitudinal band [15 W-120 E] separately in July and January

the maximum surface MSE lies equatorward side of the maximum daily insolation with a phase lag. When $C = 4.0 \times 10^7 Jm^{-2}K^{-1}$, which corresponds to a relaxation time $\tau \sim 300$ days, the maximum surface MSE lies significantly equatorward of the maximum daily insolation with a phase lag of ~ 2.5 months. This general feature of an

equatorward shift of the maximum surface MSE from the maximum daily insolation is consistent for various obliquities such as a lower obliquity of 10° (Fig. 6a1) and two higher obliquities of 32° (Fig. 6c1) and 40° (Fig. 6d1). The effect of heat capacity can be easily understood from the solution to the local energy balance model as

$$T_S(t) = \frac{\exp(-t/\tau)}{C} \int_0^t \exp(t'/\tau) \left[Q_t(t')(1-\alpha) - A \right] dt'. \tag{4}$$

Now, the migration of the maximum surface temperature follows the maxima of accumulated insolation over a thermal inertia time scale τ which is weighted by the $\exp(t'/\tau)$, rather than the maximum daily insolation. Since the surface MSE is calculated as a function of surface temperature, we can argue that heat capacity, as a leading effect, tends to limit the maximum surface MSE to a latitude lower than the maximum daily insolation, with a phase delay. This is also the case in the $\operatorname{CESM}_{\operatorname{SOM}}$ simulations. It helps us understand how the difference between the heat capacities of land (like $C = 1.0 \times 10^7 Jm^{-2} K^{-1}$) and ocean (like $C = 4.0 \times 10^7 Jm^{-2}K^{-1}$) contributes to the difference between the positions of the maximum surface MSE over land and ocean, similarly but more clearly than the previous studies shown in GCMs (Xie 2004; Bordoni and Schneider 2008; Donohoe et al. 2014).

Factor 2: surface albedo

The increased surface albedo towards high latitudes further limits the poleward migration of the maximum surface MSE. This can be seen in the idealized simulations "EBM_local_a" (Table 2, Fig. 6a2, b2, c2, d2), adopting the latitudinally-varied surface albedo (Fig. 3a2, b2, c2 and d2). Taking the model with $C = 1.0 \times 10^7 Jm^{-2}K^{-1}$ as an example, in comparison with the "EMB_local" (red lines in Fig. 6a1, b1, c1, and d1), the maximum surface MSE in all the simulations of "EMB_local_a" but "EMB_ local_a_40" (red lines in Fig. 6a2, b2, and c2) are remarkably shifted equatorward in local summers. This occurs because the high albedo of ice/snow at high latitudes in those cases greatly reduces the insolation received on the local surface and consequently performs a further limitation of poleward extension of maximum surface MSE in addition to the effect of heat capacity (Factor 1). It also can be proven from the other side where the maximum surface MSE in boreal summer of "EMB_local_a_40" stays in Arctic as well as in "EMB_local_40", because of roughly uniform small surface albedo towards high latitudes due to the sea ice melting. Similar conclusions can be drawn from the simulations of the model with heat capacities of $0.1 \times 10^7 Jm^{-2}K^{-1}$ (blue lines in Figs. 6a2, b2, and c2) and $4.0 \times 10^7 Jm^{-2} K^{-1}$ (green lines in Fig. 6a2, b2, and c2).



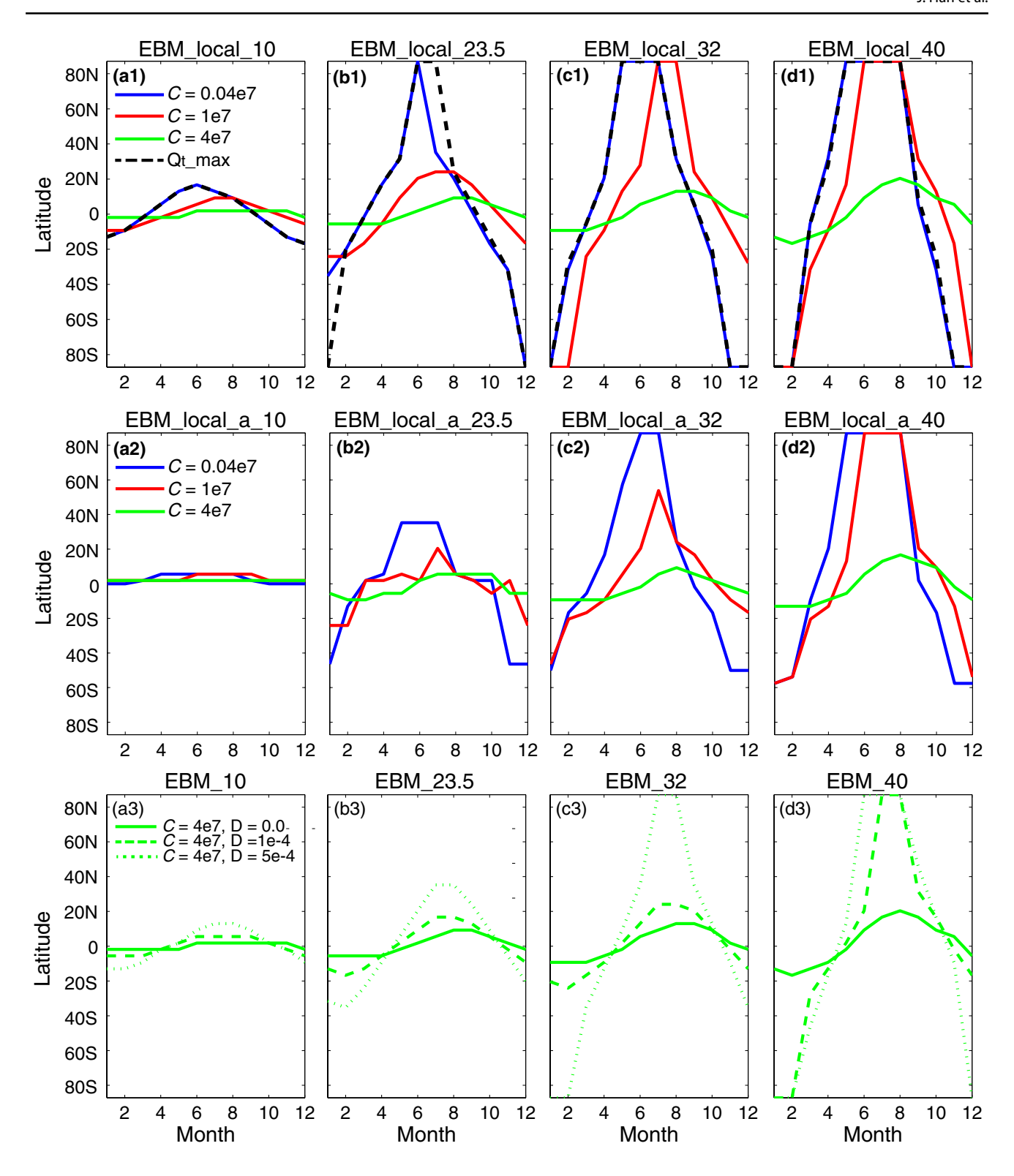


Fig. 6 Seasonal cycle of the latitude of the maximum surface moist static energy (MSE) for the simulations "EBM_local" (top row), "EBM_local_a" (middle row), and "EBM" (bottom row) in Table 2. Top row (**a1-d1**), in each diagram, blue, red, and green solid lines indicate the positions of maximum surface MSE of the simulation with the heat capacity C of 0.04×10^7 , 1.0×10^7 , and $4.0 \times 10^7 Jm^{-2}K^{-1}$, respectively. The black dashed line shows the lati-

tude of the maximum daily insolation $Q_{t,\max}$ in each obliquity experiment, same as the black solid lines in Fig. 3a1, b1, c1, and d1. Middle row (**a2-d2**), as similar as (**a1-d1**), but the surface albedo is latitude-dependent whose distribution is shown separately in Fig. 3a2, b2, c2, and d2. Bottom row (**a3-d3**), the green solid lines (D=0) are the same as the green solid lines in top row; the green dashed and dotted lines are for $D=1\times10^{-4}$ and 5×10^{-4} kgm⁻²s⁻¹, respectively



Factor 3: meridional MSE transport

Different from the above two factors, poleward MSE transport at certain latitude tends to increase the net energy input at higher latitudes, which may therefore shift the position of maximum surface MSE poleward in the simulations of "EBM_local" (see Appendix A), certainly for a case where the maximum surface MSE does not reach the poles yet. This is confirmed with the simulations "EBM" (Table 2, Fig. 6a3, b3, c3, and d3), which adopts a finite diffusivity D > 0. Under the idealized condition of a spatially uniform positive diffusivity and surface albedo, meridional MSE transport shifts the maximum surface MSE (not lying at the summer pole) poleward with increasing diffusivity D and forces the maximum surface MSE more in phase with the insolation forcing (Fig. 6a3, b3, c3 and d3). If the maximum surface MSE reaches the pole as the obliquity is increased to a certain value, based on the analysis in Appendix A, we can speculate that the effect of increasing the efficiency of the meridional MSE transport may become the opposite as what is seen in relatively lower obliquity, shifting the maximum surface MSE equatorward.

It should be noted that while a uniform *D* may simulate the extratropical eddy heat transport well, it may underestimate the heat transport by the mean circulation in the tropics due to the small temperature gradient there. *D* should be larger in the regions of the mean heat transport dominated by Hadley cells than of the eddy heat transport dominating (Lindzen and Farrell 1977; Stone 1978; North et al. 1983; Mbengue and Schneider 2018). However, it remains unclear how the intensity and extent of Hadley cells and eddies covary with increasing obliquity and, furthermore, how their intensity is related to *D* quantitatively. It is beyond the scope of this work to give a realistic distribution of *D* for each case. Therefore, we confine our study to the case of uniform diffusivity here, which, nevertheless, is still able to help us illustrate the effect of heat transport qualitatively.

It should also be noted that this conceptual model can not emulate the ventilation effect (Chou and Neelin, 2001, 2003) in the CESM_{SOM} since the simple model is assumed to be zonally homogeneous. The poleward expansion effect of meridional MSE transport above is in the meridional direction, while the ventilation effect is dominated by the zonal advection.

The Budyko-Sellers energy balance model study above sheds some lights on the mechanisms that control the seasonal poleward migration of maximum surface MSE Θ_{mp} . The migration of maximum precipitation ϕ_{mp} can be understood similarly if we assume the ϕ_{mp} in the simple model always coincides with the Θ_{mp} , as in the present-day observation and our CESM_{SOM} simulation. Therefore, heat capacity is the primary mechanism that controls ϕ_{mp} . A finite heat capacity leads to the maximum surface MSE Θ_{mp} and, in

turn, ϕ_{mp} , migrating less poleward than the maximum daily insolation with a phase lag. As secondary effects, the poleward increasing surface albedo further limits the poleward migration of Θ_{mp} and, in turn, ϕ_{mp} , but the poleward MSE transport represented here by constant diffusivity expels the maximum surface MSE (not yet reaching the poles) and, in turn, ϕ_{mp} poleward. These three effects, we think, are probably among the essential controls that determine the latitudes of the Θ_{mp} and ϕ_{mp} in the more complex models and perhaps real world, while other mechanism, such as the effects of variable relative humidity, cloud albedo and cloud cover, could also play some role.

4.2 Understanding from the CESM_{SOM}

The Budyko-Sellers model study suggests some fundamental controls on the poleward extent of seasonal migration for the continental maximum precipitation ϕ_{mp} and maximum surface MSE Θ_{mp} , based on the assumption that the ϕ_{mp} and Θ_{mp} always coincide. However, the ϕ_{mp} , which is calculated explicitly from the precipitation field, actually lies far equatorward of the Θ_{mp} in our CGCM experiments of high obliquity. It is therefore interesting to explore what causes the separation between the positions of maximum precipitation ϕ_{mp} and maximum surface MSE Θ_{mp} over land, and also between the positions of ϕ_{ocn} and Θ_{ocn} over ocean, under high obliquities. This question is studied in this subsection with CESM_{SOM}, which relaxes the assumption that the ϕ_{mp} always co-locates with Θ_{mp} .

The free-tropospheric weak temperature gradient has been the prerequisite to use the latitude of maximum surface MSE Θ_{mp} (Θ_{ocn}) to predict the location of maximum precipitation ϕ_{mp} (ϕ_{ocn}) over a seasonal cycle in our CGCM experiments, as argued in previous studies about the present-day mean ITCZ and zonal-mean maximum surface MSE (e.g. Nie et al. 2010). The equatorial Rossby radius determines the poleward extent to which atmospheric waves can adjust the tropical free-tropospheric temperature effectively to achieve weak horizontal gradients. However, the equatorial Rossby radius

$$L_c = \left(\frac{c}{\beta}\right)^{1/2} \tag{5}$$

is inversely proportional to the square root of rotation rate Ω as the meridional gradient of the Coriolis parameter $\beta \propto \Omega$. Thus, it is conceivable that rotation rate can be a factor that limits ϕ_{mp} behind the Θ_{mp} because of its constrain on the latitude extent of the weak free-tropospheric temperature gradients. This conclusion has been confirmed in the CESM_{SOM} "Rotation Experiments" (Table 1), where the rotation rate is reduced from twice down to 1/8th of the current Earth's rotation rate (Ω_E). The results of the experiments with the



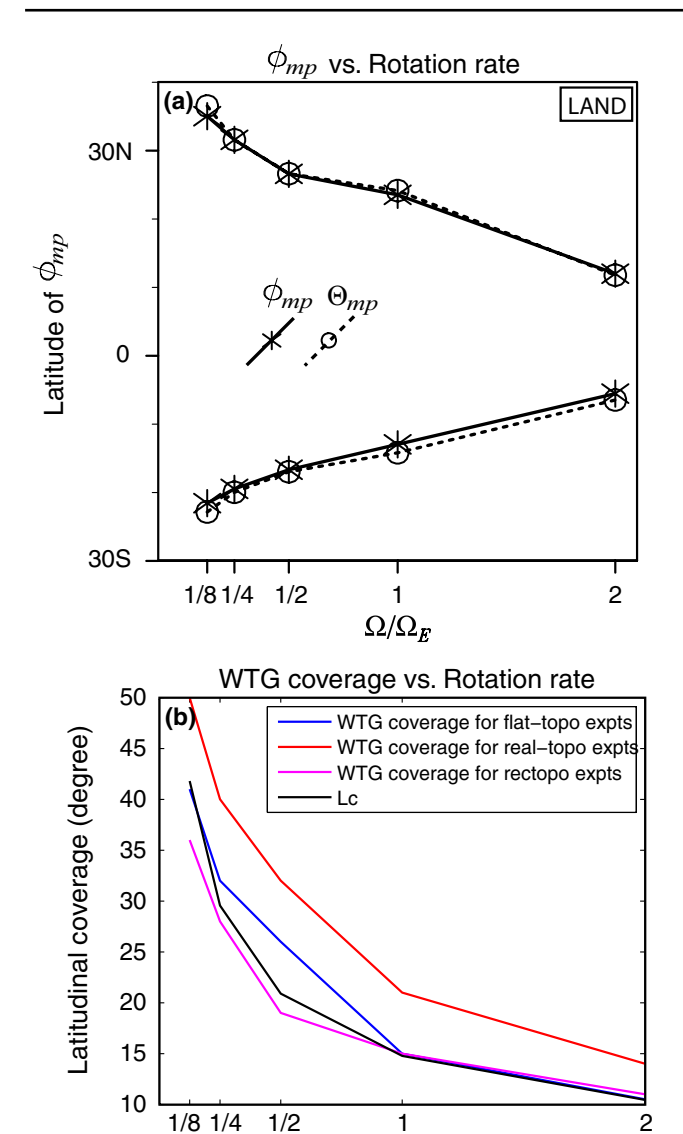


Fig. 7 Top panel **a**, seasonal migration of ϕ_{mp} (solid line with asterisks) and Θ_{mp} (dashed line with circles) versus rotation rate, averaged over summer (JJA) and winter (DJF) in "Rotation Experiments": Obliq23.5_ $\Omega_E/8$, Obliq23.5_ $\Omega_E/4$, Obliq23.5_ $\Omega_E/2$, Obliq23

 Ω/Ω_E

extremely low rotation rate $\Omega_E/8$ are incorporated in Fig. 4 and the results of other rotation rate cases will be shown in Fig. 7a. When the rotation rate is decreased to $\Omega_E/8$, the ϕ_{mp} in both hemispheres (red asterisks in Fig. 4a1, a2, a3, and a4) migrate poleward under various obliquities, even to the poleward latitudinal boundary of the Eurasian continent in

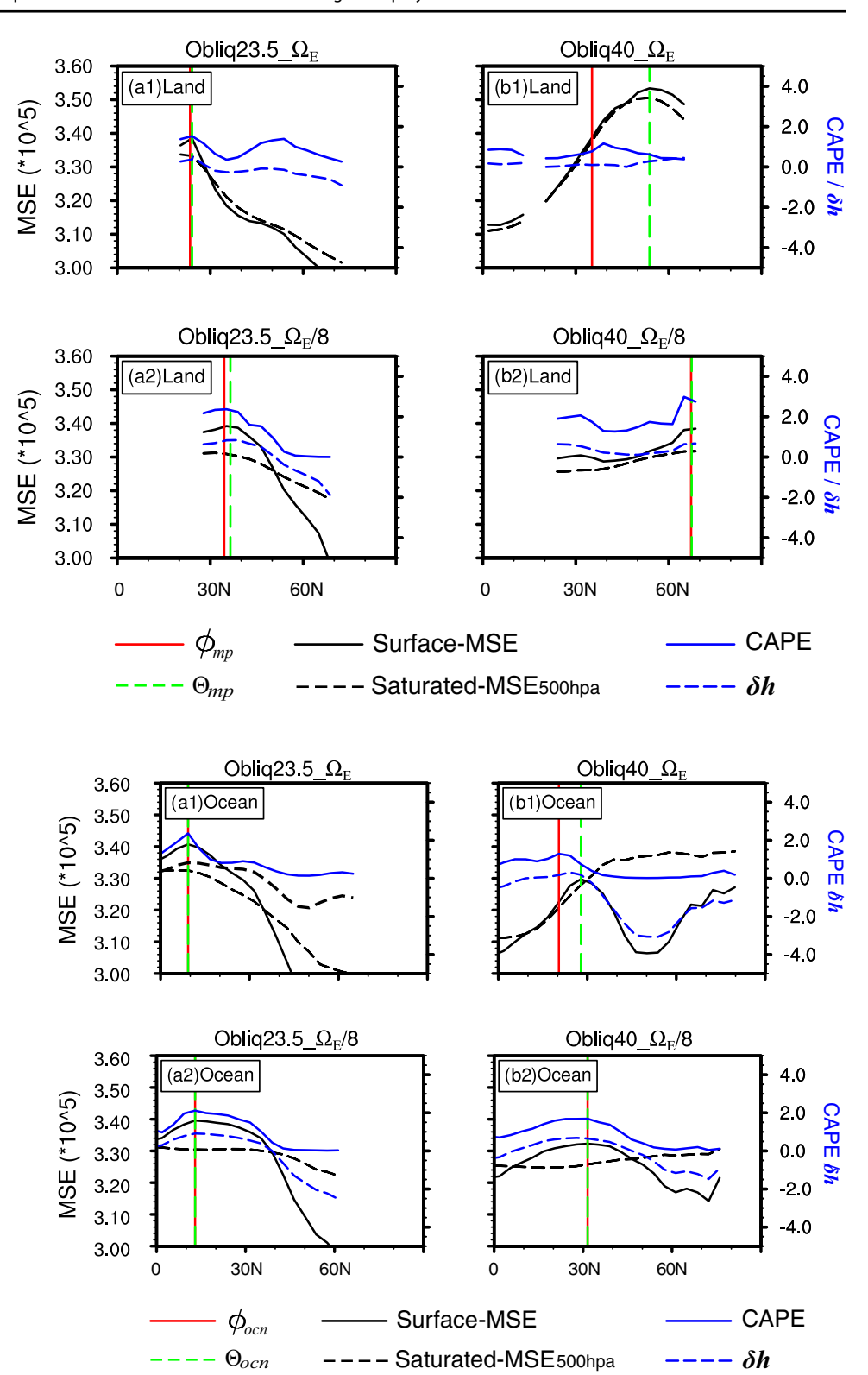
June for obliquity 40°. The ϕ_{mn} in the Northern Hemisphere has a greater shift than that in the Southern Hemisphere (Figs. 4a1, a2, a3, and a4, 7a) because the latter has a small land coverage and therefore is influenced more by the ocean and, in turn, the ventilation as discussed above. A comparison between the experiments of the rotation rates of Ω_E and $\Omega_F/8$ shows that, for the low obliquities, ϕ_{mp} remains coincident with the latitude of maximum surface MSE Θ_{mn} at the two different rotation rates (Fig. 4a1 and a2); under the high obliquities, the separation between ϕ_{mp} and Θ_{mp} is reduced with reduced rotation rate (Fig. 4a3 and a4). This happens because weak temperature gradients in the free troposphere is limited within the tropics by the Earth's rotation rate, and therefore can expand to higher latitudes with a reduction in the rotation rate, and, in turn, an increase in equatorial Rossby radius. Figure 7b shows the scaling of the latitudinal coverage of weak temperature gradients with different rotation rates. The boundary of the weak temperature gradient here is gained visually as the latitude where zonal-mean temperature first rapidly changes in the meridional direction. It is seen that the latitudinal coverage of weak temperature gradients increases with the reduction of the rotation rate, roughly following the change of the equatorial Rossby radius (blue line in Fig. 7b) where $c \approx 50 \text{m/s}$ for the first baroclinic mode of tropical troposphere. A similar scaling is also found in the parallel experiments of CESM_{SOM} with realistic topography (red line in Fig. 7b) and with a rectangular sea-land configuration (magenta line in Fig. 7b). The correlation coefficient between the coverage of WTG and equatorial Rossby radius over a 16-fold variation in rotation rate exceeds 0.98.

The relation between the WTG and rotation rate and the relation between the positions of maximum precipitation $\phi_{mp}(\phi_{ocn})$ and maximum surface MSE $\Theta_{mp}(\Theta_{ocn})$ discussed above can also be diagnosed from the latitudinal distribution of atmospheric moist static energy. We first verify the use of CAPE and the difference between surface MSE and upperlevel saturated MSE (denoted as " δh " hereafter) to infer conditional instability in the atmospheric column as discussed in Sect. 1. This thermodynamic mechanism is largely valid in our CESM_{SOM} experiments under various obliquities and rotation rates: a maximum CAPE/ δh corresponds to a maximum precipitation (Figs. 8, 9). We just show the results of the simulations with the obliquities of 23.5° and 40° and rotation rates of Ω_E and $\Omega_E/8$, since the cases of obliquity 10° and 32° obtain results similar to the cases of obliquity 23.5° and 40°, respectively. It is noted that the δh performs not quite well as the CAPE as a prediction of the position of ϕ_{mn} in the case of high obliquity 40° at the Earth rotation rate (Fig. 8b1). This is likely due to variations in lapse rate in the free troposphere making the two quantities not correlate exactly. Nevertheless, the δh is confirmed to linearly correlate with CAPE with a correlation coefficient of 0.85.



Fig. 8 Latitudinal distributions in July, of surface moist static energy (black solid lines, left vertical coordinate, unit: 10⁵ J kg⁻¹), 500hpa saturated moist static energy (black dashed lines, left vertical coordinate, unit: 10⁵ J kg⁻¹), their difference (δh , the former minus the latter, blue dashed lines, right vertical coordinate, unit: 10⁴ J kg⁻¹), convective available potential energy (CAPE, blue solid lines, right vertical coordinate, unit: 10² J kg⁻¹), at the rotation rates of Ω_E (a1, b1) and $\Omega_E/8$ (a2, b2) with obliquity 23.5° and 40°. All of these variables are zonally averaged over the longitudes where the three poleward-most points over land contributing to the ϕ_{mp} are located. Red solid vertical lines show the positions of ϕ_{mn} in July; green dashed vertical lines show the positions of maximum surface MSE Θ_{mn} in July

Fig. 9 As Fig. 8, but for the marine case. Variables are zonally averaged over the sections covered by ocean. Red solid vertical lines show the positions of ϕ_{ocn} in July; green dashed vertical lines show the positions of maximum surface MSE Θ_{ocn} in July



Furthermore, we know, due to a weak meridional gradient of upper-level saturated MSE in the present-day climate, one can use the maximum surface MSE only, instead of CAPE or δh , to predict the tropical deep conditional instability and

thus present-day ITCZ's position. Analogously, we apply this theory to the ϕ_{mp} . We take the summer results as an example. Figure 8a1 and b1 show the latitudinal distribution of the continental surface MSE (black solid lines) and



500hpa-saturated MSE (black dashed lines) zonally averaged over the corresponding longitudes of the three polewardmost points that contribute to the ϕ_{mv} . It is obvious that the ϕ_{mn} (red vertical line) coincides with the latitude of maximum surface MSE Θ_{mn} (green vertical line) in a low obliquity case where Θ_{mp} falls within the coverage area of weak temperature gradients, which are shown by the flat feature of the 500 hpa-saturated MSE line (black dashed lines in Fig. 8a1). But the ϕ_{mp} is separated significantly away from the Θ_{mp} in a high obliquity case, where the WTG are constrained within the tropics (black dashed lines in Fig. 8b1) behind the Θ_{mn} located at high latitudes. When the rotation rate is decreased from Ω_E to $\Omega_E/8$, the adjustment to weak horizontal gradients of upper-level tropospheric saturated MSE (black dashed lines in Fig. 8a2 and b2) occurs on a larger scale and therefore allows the ϕ_{mn} to coincide with the Θ_{mn} under high obliquities (Fig. 8b2). This theory also holds over the ocean between the positions of ϕ_{ocn} and Θ_{ocn} (Fig. 9).

The mechanism of rotation on limiting the seasonal shift of land precipitation maxima ϕ_{mp} may also be understood from the axisymmetric theory, although this theory neglects the effect of eddy on the mean circulation and was designed specifically to predict the latitude of the ascending branch of solstitial Hadley circulation (SHC) rather than the ϕ_{mn} (Lindzen and Hou 1988; Caballero et al. 2008; Guendelman and Kaspi 2018; Hill et al. 2019; Singh 2019). Due to the combination of angular-momentum conservation and thermal wind assumptions, the dependence of the ascending branch latitude on the rotation rate is emphasized by the expression of the thermal Rossby number. The position of the ascending branch shifts poleward with decreasing rotation rate. In addition, the rotation rate dependence of the ϕ_{mn} may be also understood from an energy flux perspective. The effect of rotation can affect the meridional heat transport and in turn the precipitation. So far, most studies on the rotation effect on heat transport has focused on the annual mean transport. Nevertheless, these studies may shed some light on the seasonal response case here. In the tropics, a reduction of rotation rate expands the Hadley cells and then increases the meridional heat transport by the mean circulation (Held and Hou 1980; Walker and Schneider 2006; Kaspi and Showman 2015). This is similar to the case of increased diffusivity in the Budyko-Sellers model, favoring the poleward extension of precipitation. In the extratropics, poleward eddy heat transport can increase when the rotation rate decreases, because eddies are enlarged due to the increased Rossby deformation radius $(L_D \propto \Omega^{-1})$ and are more effective in transporting heat (Kaspi and Showman 2015; Liu et al. 2017). This is somewhat equivalent to the effect of an increased diffusivity in the Budyko-Sellers model, also leading to a poleward shift of precipitation. This interpretation of the rotation rate on displacing the latitude of precipitation maxima through varying diffusivity, of course, remains qualitative and requires further study.

5 Conclusions and discussions

The seasonal response of the poleward extension of continental precipitation maxima to high obliquity is studied using a CGCM and an idealized energy balance model. In particular, we have focused on the extreme latitudinal shift of the continental monsoon precipitation maxima, denoted as the ϕ_{mp} . The advection of low moist enthalpy from ocean into the continent, namely the ventilation effect, works to limit the poleward edge (the 2 mm/day contour) of monsoonal rainfall in our CGCM obliquity experiments and provides an upper bound for the maxima's shifts but can not quantitatively predict the latitude of ϕ_{mp} .

In the set of CGCM experiments with increasing obliquity from 10° to 23.5°, 32° and eventually 40°, the extent of the seasonal migration of ϕ_{mp} increases as expected, gradually from 5 S-10 N to 30 S-35 N. However, the poleward extent of ϕ_{mp} is always confined equatorward of the latitude of maximum daily insolation. This equatorward confinement of precipitation maxima is understood in an energy balance model thermodynamically, under the assumption that the latitude of maximum precipitation over land (ϕ_{mp}) coincides with the position of its corresponding maximum surface MSE (Θ_{mn}) , as in the present day observation and pre-industrial simulation of CGCM. The suppression of the poleward extent of ϕ_{mp} relative to the latitude of maximum daily insolation is caused primarily by a finite heat capacity, which determines the surface temperature maximum co-locates the maximum of accumulated insolation over a thermal relaxation time scale. An increased heat capacity damps the response of the surface temperature and, in turn, surface MSE to insolation, suppressing the poleward migration of ϕ_{mn} and inducing a phase lag. This large heat capacity also largely explains the equatorward confinement of maximum precipitation over ocean relative to that over land, in the CGCM experiments. In addition, an increased surface albedo toward high latitudes can further limit the poleward migration of ϕ_{mp} . In the meantime, when the maximum surface MSE Θ_{mp} is not located at the summer pole, the poleward MSE transport tends to expel the ϕ_{mn} poleward, at least for the ideal condition of uniform positive diffusivity and surface albedo.

In the CGCM, the assumption of the latitude of maximum precipitation over land ϕ_{mp} coinciding with the latitude of maximum surface MSE Θ_{mp} holds well under low obliquities, such as 10° and 23.5° , which allows us to understand the CGCM's results from the energy balance model. For higher obliquities in the northern hemisphere,



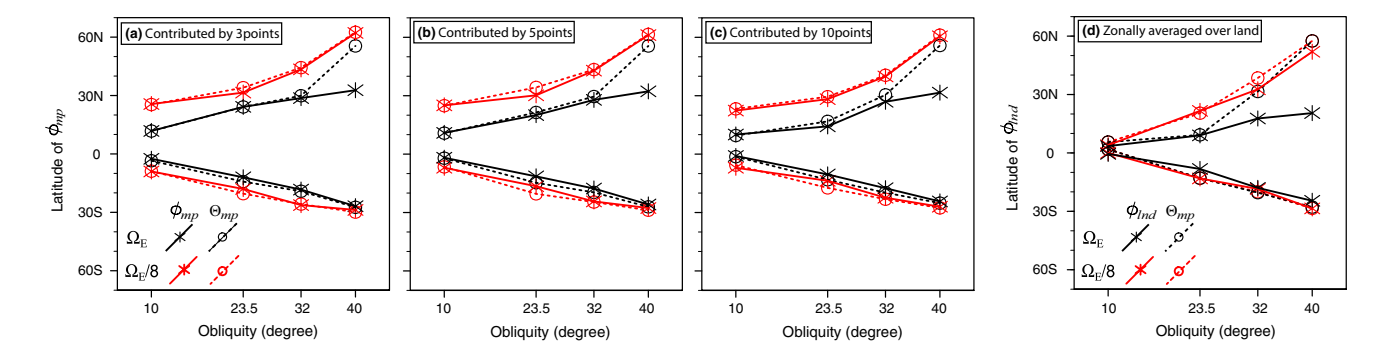


Fig. 10 a Summary for the seasonal migration of ϕ_{mp} (solid lines with asterisks) and Θ_{mp} (dashed lines with circles) versus obliquity, averaged over summer (JJA) and winter (DJF) in "Obliquity Experiments" both at the rotation rates of Ω_E (black lines and markers) and $\Omega_E/8$ (red lines and markers). **b, c** As (**a**) but for the ϕ_{mp} separately

defined by 5 and 10 poleward-most land precipitation maxima points. **d** As (**a**) but for the seasonal migration of zonally averaged land precipitation maxima ϕ_{lnd} (solid lines with asterisks) and zonally averaged surface MSE maxima Θ_{lnd} (dashed lines with circles) versus obliquity

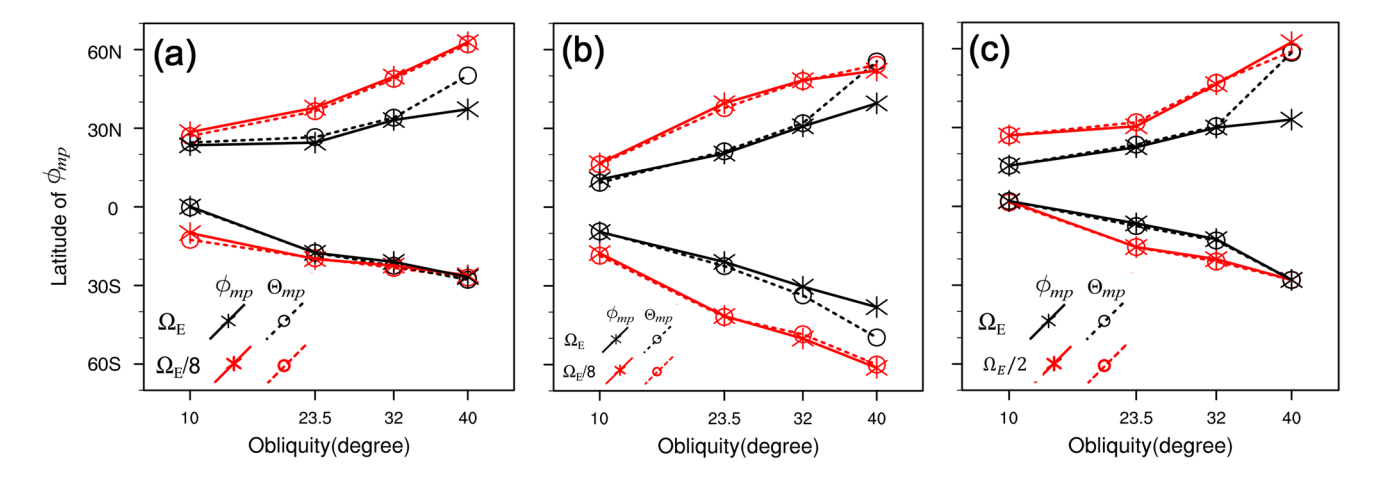


Fig. 11 As Fig. 10, but for the $CESM_{SOM}$ simulations with realistic topography (a), the $CESM_{SOM}$ simulations with rectangular sea-land configuration (b), the $CESM_{POP}$ simulations with flat topography (c)

especially of 40°, however, ϕ_{mp} lies equatorward of Θ_{mp} . This equatorward lag of the ϕ_{mp} from Θ_{mp} is interpreted as being caused by the effect of Earth's rotation on the domain of the weak temperature gradients in the tropics. The coverage of the horizontal weak temperature gradients, which is the prerequisite to use the Θ_{mp} to predict the ϕ_{mn} 's location, is constrained by the effect of rotation on the scale of equatorial Rossby radius. A decrease of the rotation rate leads to a poleward expansion of the domain of weak temperature gradients and, eventually, at very small rotation rate, allows the ϕ_{mp} to coincide with the Θ_{mp} under high obliquities. For the southern hemisphere, however, there is almost no separation between ϕ_{mp} and Θ_{mp} through all the obliquity cases, presumably due to the ϕ_{mp} always lying within an equatorial Rossby radius.

It should be pointed out that our conclusions remain robust regardless of the detailed metric (the number of points) we choose to define ϕ_{mp} . First, as pointed out earlier, in the observation, this metric is insensitive to the dataset's resolution in comparison of the three types of precipitation observational datasets (not shown). Secondly, we have repeated our analysis of the seasonal shifts of the ϕ_{mn} defined by the top 5 and 10 mostpoleward land precipitation maxima points, and, even, maximally, the zonally averaged continental precipitation maximum, denoted as " ϕ_{lnd} ", under different obliquities (Fig. 10b-d). All of our major conclusions remain similar to the case of the ϕ_{mp} defined by 3 points (Fig. 10a). Different definitions of the most poleward points do sometimes lead to the "bounce around" of some land points where different regional dynamics might be relevant. Yet, our conclusion of the relative position of ϕ_{mp} and Θ_{mp} remains robust. This suggests that our results are not sensitive to the detailed regional dynamics, instead, it is a general feature of the climate system. Finally, our



conclusions are found also valid in parallel experiments in the CESM_{SOM} with realistic topography (Fig. 11a), in the CESM_{SOM} with a rectangular sea-land distribution (Fig. 11b), and in the CESM_{POP} that incorporates ocean dynamics (Fig. 11c). Therefore, our conclusions are also robust with respect to topography, sea-land distribution and ocean dynamics (or Q-flux changes).

It should be noted that our interpretation of the limitation of rotation to the poleward migration of ϕ_{mp} from the perspectives of energy transport remains tentative. A recent study (Liu et al. 2017) explored the mechanism behind the effect of rotation on the change of meridional heat transport. If we can combine Liu's theory with the energetic argument of the mean ITCZ, it is possible to understand the mechanism behind the effect of rotation on ϕ_{mp} . Liu et al. (2017) argues that the equivalent diffusivity increases with the decrease in the rotation rate when the meridional heat transport is parameterized by the down-gradient diffusion of MSE similarly as we did in the Budyko-Sellers diffusive model. However, the summer diffusivity in our CESM_{SOM} does not increase monotonically with the reduced rotation rate (not shown). Therefore, what exactly is the mechanism by which rotation affect ϕ_{mp} seasonally remains to be further explored.

Acknowledgements We would like to thank Zachary Hansen for editing assistance. The first author is grateful for the financial support from China Scholarship Council. This work is supported by National Natural Science Foundation of China (NSFC41630527) and US National Science Foundation (NSF P2C2 AGS1810682) and Climate Dynamics AGS1656907.

Appendix A: Decomposition of the diffusion term in the Budyko-Sellers model

We decompose the diffusion term in the Budyko-Sellers energy balance model into two terms as Eq. (6) shows.

$$\frac{d}{dx} \left[D(1 - x^2) \frac{dH(x, t)}{dx} \right] = -2Dx \frac{dH}{dx} + D(1 - x^2) \frac{d^2H}{dx^2}$$
 (6)

The first term on the right-side hand of Eq. (A1) results from the spherical geometry while the second term is the divergence of MSE gradient. The 2nd term is the standard diffusion term and will smooth out the peak of MSE without shifting the location of the peak. The first term, however, is equivalent to a MSE advection term $-v\frac{dH}{dx}$ with the equivalent advection speed as v = 2Dx. Since the diffusivity D is set to be positive, the direction of the equivalent advection velocity 2Dx is always poleward, and therefore will shift the maximum MSE poleward. Physically, a latitude band has a larger area in the lower latitude than in the higher latitude. Therefore, a grid point is heated more in the high

latitude than in lower latitude when the same amount of heat is diffused towards both sides, leading to a poleward shift of the MSE peak.

Appendix B: The mean ITCZ's response to high obliquity

The mean ITCZ, defined as the latitude of maximum zonal-mean precipitation, migrates further poleward with increasing obliquity as similar as the ϕ_{mp} and ϕ_{ocn} do (Fig. 12). The mean ITCZ seasonally coincides with the maximum zonal-mean surface MSE under low obliquities and become greatly separated under high obliquities. This separation under high obliquities is eliminated by decreasing rotation rate from Ω_F to $\Omega_F/8$.

Except for the maximum surface MSE, we have assessed other two predictors for the mean ITCZ, namely the latitudes of the division between the winter- and summer- Hadley cells which is referred to as Hadley cell division (HCD) and energy flux equator (EFE). The location of HCD is determined as the latitude where the mass flux streamfunction at the pressure level of its extremum equals zero. The EFE is defined as Kang et al. (2008) did, where the zonal- and

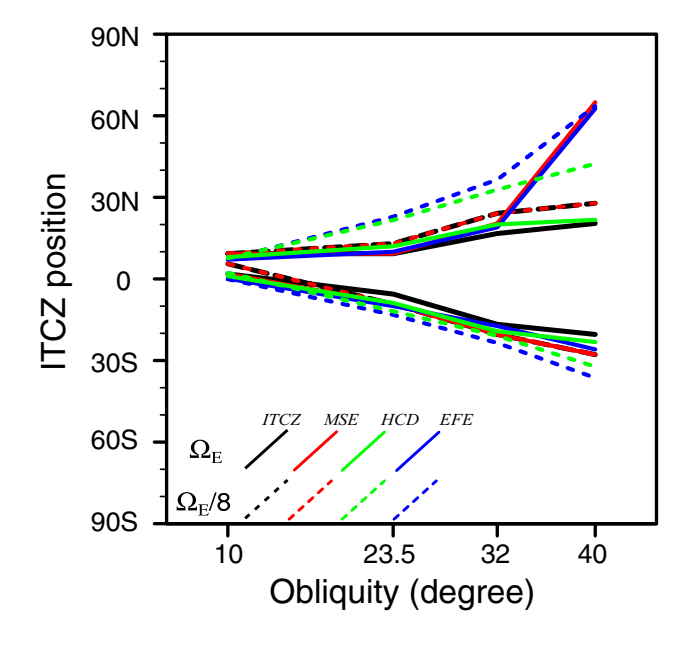
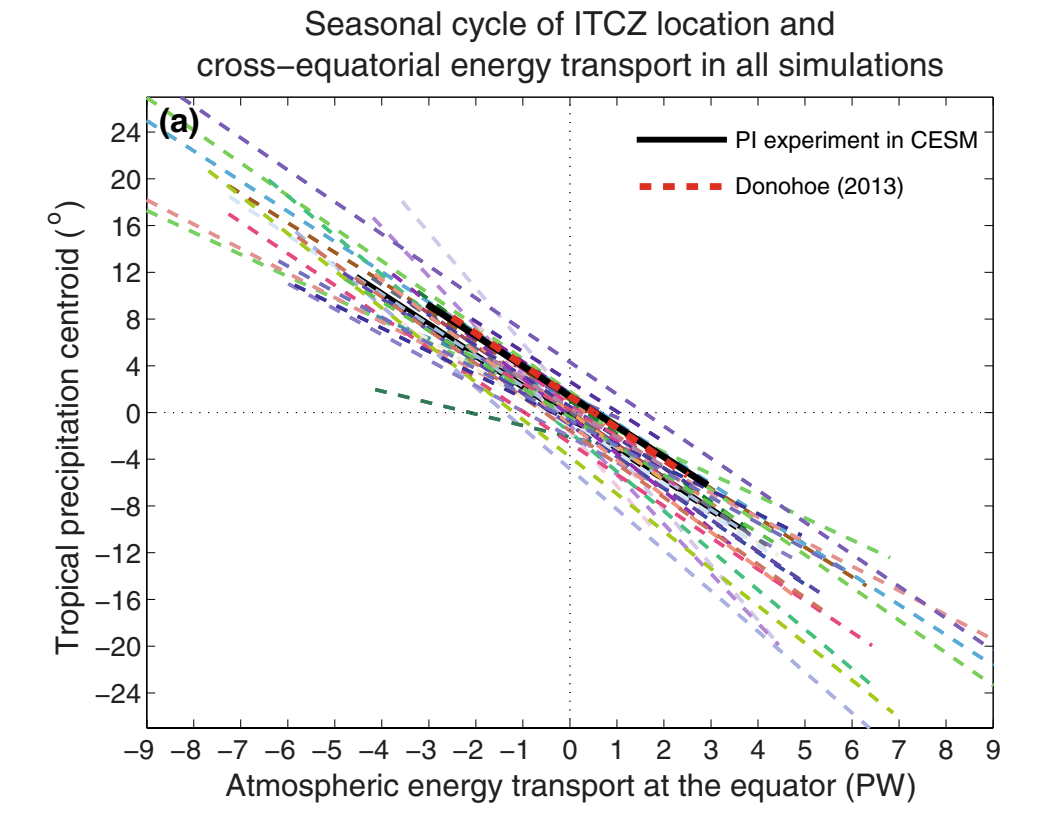
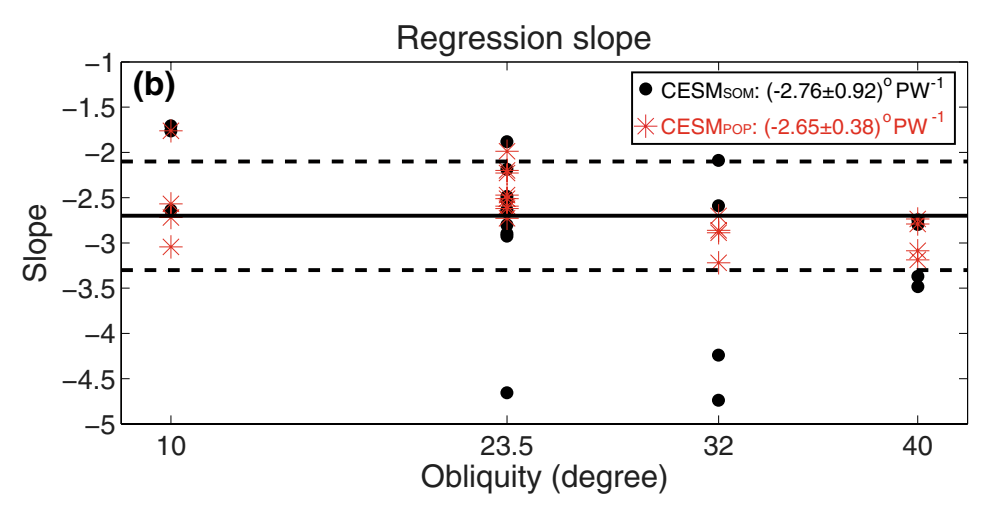


Fig. 12 Summary of the mean ITCZ's seasonal migration versus obliquity, averaged over summer (JJA) and winter (DJF) in "Obliquity Experiments" both at the rotation rate of Ω_E and $\Omega_E/8$. Black solid lines indicate the mean ITCZ's position; red solid lines, the maxima's position of zonal-mean surface moist static energy; green solid lines, the position of division between the winter- and summer- Hadley cells (HCD); blue solid lines, the position of energy flux equator (EFE), for "Obliquity Experiments" at the rotation rate of Ω_E . Those dashed lines indicate the same variables as the same color lines but for the rotation rate of $\Omega_E/8$



Fig. 13 Top panel (a), fitting curves for seasonal cycle of the mean ITCZ's position to cross-equatorial atmospheric energy transport (AET_{EQ}) in all the CESM experiments with the realistic land geometry. All the lines are the linear best fits to the monthly data, in a least squares sense. The thick black solid line is the result from the CESM pre-industrial run, which is comparable with that given by Donohoe et al. (2013) (thick red dashed line). Bottom panel (b), scatterplot for regression coefficients (given by the slope of those lines in the top diagram, unit: ${}^{\circ}PW^{-1}$) between the ITCZ and AET_{EO} over seasonal cycle for all experiments. Black dots indicate the slopes from CESM_{SOM} experiments whose mean value is $-2.76^{\circ}PW^{-1}$; red asterisks, from CESMPOP experiments whose mean value is $-2.65^{\circ}PW^{-1}$. The two black dashed horizontal lines give a range $(-2.7 \pm 0.6)^{\circ} PW^{-1}$ of the slope of ITCZ's position versus AET_{EQ} and the black solid line gives its mean $-2.7^{\circ}PW^{-1}$, which is given by Donohoe et al. (2013)





time- averaged vertical integral of moist static energy flux reaches zero. The mean ITCZ at present-day obliquity 23.5° in our CGCM is found to lie near the HCD and EFE as the previous studies show (Kang et al. 2008; Schneider et al. 2014; Bischoff and Schneider 2014, 2016; Adam et al. 2016a, b). In the "Obliquity Experiments" at the Earth's rotation rate Ω_E , the HCD lies slightly poleward of the ITCZ (Fig. 12). The EFE is located just poleward of the ITCZ and

coincides well with the HCD except for obliquity 40°, which is found to be related to the enhancement of tropical large-scale eddies under high obliquity. The EFE is calculated by total atmospheric meridional energy transport, including mean- and eddy- energy transport together. However, the HCD, as its definition, should be highly correlated with tropical mean energy transport. Under low obliquities, eddy energy transport in the tropics are so small that the EFE can



be approximately decided by mean energy transport, which is also supported by the previous studies (Webster and Holton 1982; Schneider and Bordoni 2008). However, under obliquity 40°, tropical eddy energy transport is not negligible which makes the EFE distant from the HCD and also from the mean ITCZ. In addition, when the rotation rate is decreased, the HCD and EFE become more separated from the ITCZ and also from each other especially in boreal summer. This separation can be understood by the definitions of the HCD and EFE which are close to the latitude at which the stream function changes sign rather than the latitude at which the meridional gradient of stream function maximizes (i.e. the latitude of maximum upward vertical velocity, corresponding to the ITCZ). The applicability of HCD and EFE to explain the mean ITCZ remains to be tested.

Additionally, we have explored the mean ITCZ's seasonal migration from the energy flux framework. When we increase the obliquity dramatically, resulted insolation variations will shift the atmospheric energy balance greatly and thereby cause the mean ITCZ's shift. Notably, Donohoe et al. (2013) quantifies the relationship between the meridional shifts of the mean ITCZ and the changes in AET_{EO}, with a regression slope of $\sim -3^{\circ}$ PW⁻¹ both in observations and in CMIP3 models. We make the same linear regression analysis of the mean ITCZ versus AET_{FO} over the seasonal cycle to reexamine that quantified relationship in our all CESM_{SOM} and CESM_{POP} experiments. The seasonal cycle of the mean ITCZ vs. AET_{EO} are significantly anticorrelated with each other in all the simulations; the larger absolute value AET_{EO} is, the farther off the equator the mean ITCZ lies (Fig. 13 top). The relationship gathered from the CESM pre-industrial experiment (thick solid black line, in Fig. 13 top) is almost the same as Donohoe got from observations and CMIP3 models (thick dashed red line, in Fig. 13 top). Furthermore, almost all the regression coefficients between the mean ITCZ and AET_{EO} from the $CESM_{POP}$ experiments (red asterisks, in Fig. 13 bottom), whose mean is $-2.65^{\circ}PW^{-1}$, lie in the interval of $(-2.7 \pm 0.6)^{\circ} PW^{-1}$ argued by Donohoe et al. (2013). However, the regression coefficients between the mean ITCZ and $\ensuremath{\mathsf{AET}}_{\ensuremath{\mathsf{EQ}}}$ from the $\ensuremath{\mathsf{CESM}}_{\ensuremath{\mathsf{SOM}}}$ experiments (black dots, in Fig. 13 bottom), whose mean is $-2.76^{\circ}PW^{-1}$, are not always located in the interval of $(-2.7 \pm 0.6)^{\circ} PW^{-1}$. We presumably attribute the difference of the coefficients between CESM_{POP} and CESM_{SOM} experiments to the influence of ocean dynamics on the energy transport, which remains to be tested. Nevertheless, the quantitative relationship ($\sim -3^{\circ}PW^{-1}$) between the mean ITCZ's shift and changes of AETEO is quite robust for the kinds of climate states in our CESM experiments, which builds a fundamental energetic constraint on the magnitude of the mean ITCZ's shift.



References

- Abbot DS, Tziperman E (2009) Controls on the activation and strength of a high-latitude convective cloud feedback. J Atmos Sci 66:519–529
- Adam O, Bischoff T, Schneider T (2016a) Seasonal and interannual variations of the energy flux equator and ITCZ. Part I: zonally averaged ITCZ position. J Clim 29:3219–3230
- Adam O, Bischoff T, Schneider T (2016b) Seasonal and interannual variations of the energy flux equator and ITCZ. Part II: zonally varying shifts of the ITCZ. J Clim 29:7281–7293
- An Z et al (2015) Global monsoon dynamics and climate change. Annu Rev Earth Planet Sci 43:29–77
- Armstrong JC, Barnes R, Domagal-Goldman S, Breiner J, Quinn TR, Meadows VS (2014) Effects of extreme obliquity variations on the habitability of exoplanets. Astrobiology 14:277–291
- Back LE, Bretherton CS (2009) A simple model of climatological rainfall and vertical motion patterns over the tropical oceans. J Clim 22:6477–6497
- Bhat GS, Srinivasan J, Gadgil S (1996) Tropical deep convection, convective available potential energy and sea surface temperature. J Meteorol Soc Jpn 74:155–166
- Bischoff T, Schneider T (2014) Energetic constraints on the position of the intertropical convergence zone. J Clim 27:4937–4951
- Bischoff T, Schneider T (2016) The equatorial energy balance, ITCZ position, and double-ITCZ bifurcations. J Clim 29:2997–3013
- Bischoff T, Schneider T, Meckler AN (2017) A conceptual model for the response of tropical rainfall to orbital variations. J Clim 30:8375–8391
- Bohren CF, Albrecht BA, Schroeder DV (1998) Atmospheric thermodynamics. Oxford University Press, New York
- Bolton D (1980) The computation of equivalent potential temperature. Mon Weather Rev 108:1046–1053
- Boos WR, Kuang ZM (2010) Dominant control of the South Asian monsoon by orographic insulation versus plateau heating. Nature 463:218–222
- Bordoni S, Schneider T (2008) Monsoons as eddy-mediated regime transitions of the tropical overturning circulation. Nat Geosci 1:515–519
- Bosmans JHC, Drijfhout S, Tuenter E, Hilgen F, Lourens L (2015) Response of the North African summer monsoon to precession and obliquity forcings in the EC-Earth GCM. Clim Dyn 44:279–297
- Bretherton CS, Smolarkiewia PK (1989) Gravity waves, compensating subsidence and detrainment around cumulus clouds. J Atmos Sci 46:740–759
- Broccoli AJ, Dahl KA, Stouffer RJ (2006) Response of the ITCZ to Northern Hemisphere cooling. Geophys Res Lett 33:L01702
- Budyko MI (1969) The effect of solar radiation variations on the climate of the earth. Tellus 21:611–619
- Caballero R, Pierrehumbert RT, Mitchell JL (2008) Axisymmetric, nearly inviscid circulations in non-condensing radiative-convective atmospheres. O J R Meteorol Soc 134:1269–1285
- Chao W, Chen BD (2001) The origin of monsoons. J Atmos Sci 58:3497–3507
- Charney JG (1963) A note on large-scale motions in the tropics. J Atmos Sci 20:607–609
- Charney JG (1969a) A further note on large-scale motions in the tropics. J Atmos Sci 26:182–185
- Charney JG (1969b) The intertropical convergence zone and the Hadley circulation of the atmosphere. Proc WMO/IUGG Symp Numer Weather Predict Jpn Meteorol Agency III:73–79
- Chen GS, Liu Z, Kutzbach JE (2014) Reexamining the barrier effect of the Tibetan Plateau on the South Asian summer monsoon. Climate Past 10:1269–1275

- Chiang JCH, Bitz CM (2005) Influence of high latitude ice cover on the marine intertropical convergence zone. Clim Dyn 25:477–496
- Chou C, Neelin JD (2001) Mechanisms limiting the southward extent of the South American summer monsoon. Geophys Res Lett 28:2433–2436
- Chou C, Neelin JD (2003) Mechanisms limiting the northward extent of the northern summer monsoons over North America, Asia and Africa. J Clim 16:406–425
- Donohoe A, Armour KC, Pendergrass AG, Battisti DS (2014) Shortwave and longwave radiative contributions to global warming under increasing CO₂. Proc Natl Acad Sci USA 111(16):700–705
- Donohoe A, Marshall J, Ferreira D, McGee D (2013) The relationship between ITCZ location and cross-equatorial atmospheric heat transport: from the seasonal cycle to the Last Glacial Maximum. J Clim 26:3597–3618
- Emanuel KA (1995) On thermally direct circulations in moist atmospheres. J Atmos Sci 52:1529–1534
- Faulk S, Mitchell J, Bordoni S (2017) Effects of rotation rate and seasonal forcing on the ITCZ extent in planetary atmosphere. J Atmos Sci 74:665–678
- Ferreira D, Marshall J, O'Gorman PA, Seager S (2014) Climate at high-obliquity. Icarus 243:236–248
- Frierson DMW, Held IM, Zurita-Gotor P (2007) A gray-radiation aquaplanet moist GCM. Part II: energy transports in altered climates. J Atmos Sci 64:1680–1693
- Frierson DMW, Hwang YT (2012) Extratropical influence on ITCZ shifts in slab ocean simulations of global warming. J Clim 25:720–733
- Frierson DMW, Hwang YT, Fuckar NS, Seager R, Kang SM, Donohoe A, Maroon EA, Liu X, Battisti DS (2013) Contribution of ocean overturning circulation to tropical rainfall peak in the northern hemisphere. Nat Geosci 6:940–944
- Guendelman I, Kaspi Y (2018) An axisymmetric limit for the width of the Hadley cell on planets with large obliquity and long seasonality. Geophys Res Lett 45:13213–13221
- Hahn D, Manabe S (1975) The role of mountains in the south Asian monsoon circulation. J Atmos Sci 33:2461–2463
- Hansen J, Fung I, Lacis A, Rind D, Lebedeff S, Ruedy R, Russell G, Stone P (1988) Global climate changes as forecast by Goddard Institute for Space Studies three-dimensional model. J Geophys Res 93:9341–9364
- Held IM, Hou AY (1980) Nonlinear axially symmetric circulations in a nearly inviscid atmosphere. J Atmos Sci 37:515–533
- Hill S, Bordoni S, Mitchell JL (2019) Axisymmetric constraints on cross-equatorial Hadley cell extent. J Atmos Sci 76:1547–1564
- Huffman GJ et al (2007) The TRMM Multisatellite Precipitation Analysis (TMPA): quasi-global, multiyear, combined-sensor precipitation estimates at fine scales. J Hydrometeorol 8:38–55
- Hwang YT, Frierson DMW (2010) Increasing atmospheric poleward energy transport with global warming. Geophys Res Lett 37:L24807
- Jenkins GS (2000) Global climate model high-obliquity solutions to the ancient climate puzzles of the faint-young Sun paradox and low-latitude Proterozoic glaciation. J Geophys Res 105:7357–7370
- Kang SM, Frierson DMW, Held IM (2009) The tropical response to extratropical thermal forcing in an idealized GCM: the importance of radiative feedbacks and convective parameterization. J Atmos Sci 66:2812–2827
- Kang SM, Held IM, Frierson DMW, Zhao M (2008) The response of the ITCZ to extratropical thermal forcing: Idealized slab-ocean experiments with a GCM. J Clim 21:3521–3532
- Kang W (2019a) Mechanisms leading to a warmer climate on high obliquity planets. Astrophys J Lett 876:1
- Kang W (2019b) Wetter stratospheres on high-obliquity planets. Astrophys J Lett 877:L6

- Kang W, Cai M, Tziperman E (2019) Tropical and extratropical general circulation with a meridional reversed temperature gradient as expected in a high obliquity planet. Icarus 330:142–154
- Kaspi Y, Showman AP (2015) Atmospheric dynamics of terrestrial exoplanets over a wide range of orbital and atmospheric parameters. Astrophys J 804:60
- Lea DW, Pak DK, Peterson LC, Hughen KA (2003) Synchroneity of tropical and high-latitude Atlantic temperatures over the last glacial termination. Science 301:1361–1364
- Lindzen RS, Farrell B (1977) Some realistic modifications of simple climate models. J Atmos Sci 34:1487–1501
- Lindzen RS, Hou AV (1988) Hadley circulations for zonally averaged heating centered off the equator. J Atmos Sci 45:2416–2427
- Linsenmeier M, Pascale S, Lucarini V (2015) Climate of Earth-like planets with high obliquity and eccentric orbits: implications for habitability conditions. Planet Space Sci 105:43–59
- Liu XD, Kutzbach JE, Liu Z, An ZS, Li L (2003) The Tibetan Plateau as amplifier of orbital-scale variability of the East Asian monsoon. Geophys Res Lett 30:1839
- Liu XJ, Battisti DS, Roe GH (2017) The effect of cloud cover on the meridional heat transport: lessons from variable rotation experiments. J Clim 30:7465–7479
- Manabe S, Stouffer RJ (1980) Sensitivity of a global climate model to an increase of CO₂ concentration in the atmosphere. J Geophys Res 85:5529–5554
- Marshall J, Donohoe A, Ferreira D, McGee D (2014) The ocean's role in setting the mean position of the Inter-Tropical Convergence Zone. Clim Dyn 42:1967–1979
- Mbengue CO, Schneider T (2018) Linking Hadley circulation and storm tracks in a conceptual model of the atmospheric energy balance. J Atmos Sci 75:841–856
- McGee D, Donohoe A, Marshall J, Ferriera D (2014) Changes in ITCZ location and cross-equatorial heat transport at the Last Glacial Maximum, Heinrich Stadial 1, and the Mid-Holocene. Earth Planet Sci Lett 390:69–79
- Neelin JD (2007) Moist dynamics of tropical convection zones in monsoons, teleconnections and global warming. In: Schneider T, Sobel A (eds) The global circulation of the atmosphere. Princeton University Press, Princeton, p 385
- Milankovitch M (1941) Canon of insolation and the ice-age problem. Israel Program for Scientific Translations, 484pp.
- Nie J, Boos WR, Kuang ZM (2010) Observational evaluation of a convective quasi-equilibrium view of monsoons. J Clim 23:4416–4428
- North GR, Mengel JG, Short DA (1983) Simple energy balance model resolving the seasons and the continents: application to the astronomical theory of the ice ages. J Geophys Res 88:6576–6586
- Nowajewski P, Rojas M, Rojo P, Kimeswenger S (2018) Atmospheric dynamics and habitability range in Earth-like aquaplanets obliquity simulations. Icarus 305:84–90
- Oglesby RJ, Ogg JG (1998) The effect of large fluctuations in obliquity on climates of the Late Proterozoic. Paleoclimates 2:293–316
- Philander SGH, Gu D, Halpern D, Lambert G, Lau NC, Li T, Pacanowski RC (1996) Why the ITCZ is mostly north of the equator. J Clim 9:2958–2972
- Riehl H (1979) Climate and weather in the tropics. Academic Press, New York
- Roe GH, Feldl N, Armour KC, Hwang YT, Frierson DMW (2015) The remote impacts of climate feedbacks on regional climate predictability. Nat Geosci 8:135–139
- Rose BE, Armour KC, Battisti DS, Feldl N, Koll DD (2014) The dependence of transient climate sensitivity and radiative feedbacks on the spatial pattern of ocean heat uptake. Geophys Res Lett 41:1071–1078



- Schneider T, Bischoff T, Haug GH (2014) Migrations and dynamics of the intertropical convergence zone. Nature 513:45–53
- Schneider T, Bordoni S (2008) Eddy-mediated regime transitions in the seasonal cycle of a Hadley circulation and implications for monsoon dynamics. J Atmos Sci 65:915–934
- Sellers WD (1969) A climate model based on the energy balance of the earth-atmosphere system. J Appl Meteorol 8:392–400
- Singh MS (2019) Limits on the extent of the solstitial Hadley cell: the role of planetary rotation. J Atmos Sci. https://doi.org/10.1175/ JAS-D-18-0341 1
- Sobel AH, Nilsson J, Polvani LM (2001) The weak temperature gradient approximation and balanced tropical moisture waves. J Atmos Sci 58:3650–3665
- Stager JC, Ryves D, Chase B, Pausata FSR (2011) Catastrophic drought in the Afro-Asian monsoon region during Heinrich Event 1. Science 331:1299–1302
- Stone PH (1978) Constraints on dynamical transports of energy on a spherical planet. Dyn Atmos Oceans 2:123–139
- Takahashi K, Battisti DS (2007) Processes controlling the mean tropical Pacific precipitation pattern. Part I: the Andes and the eastern Pacific ITCZ. J Clim 20:3434–3451
- Trenberth KE, Hurrell J, Stepaniak D (2006) The Asian monsoon: Global perspectives. In: Wang B (ed) The Asian monsoon. Springer, Praxis, pp 67–87
- Tuenter E, Weber S, Hilgen F, Lourens L (2003) The response of the African summer monsoon to remote and local forcing due to precession and obliquity. Glob Planet Chang 36:219–235
- Walker C, Schneider T (2006) Eddy influences on Hadley circulations: simulations with an idealized GCM. J Atmos Sci 63:3333–3350
- Wang B (1994) Climatic regimes of tropical convection and rainfall. J Clim 7:1109–1118
- Wang B, Bao Q, Hoskins B, Wu GX, Liu Y (2008) Tibetan Plateau warming and precipitation changes in East Asia. Geophys Res Lett 35:L14702
- Wang B, Ding QH (2008) Global monsoon: dominant mode of annual variation in the tropics. Dyn Atmos Oceans 44:165–183

- Wang PX (2009) Global monsoon in a geological perspective. Chin Sci Bull 54:1113–1136
- Wang PX, Wang B, Cheng H, Fasullo J, Guo ZT, Kiefer T, Liu Z (2014) The global monsoon across timescales: coherent variability of regional monsoons. Clim Past 10:2007–2052
- Wang Y et al (2016) Effects of obliquity on the habitability of exoplanets around M Dwarfs. Astrophys J Lett 823:L20
- Webster PJ, Holton JR (1982) Cross-equatorial response to middlelatitude forcing in a zonally varying basic state. J Atmos Sci 39:722–733
- Webster P, Fasullo J (2003) Monsoon: dynamical theory. Encyclopedia of Atmospheric Sciences, Vol. 3, Academic Press, 1370–1391
- Williams DM, Pollard D (2003) Extraordinary climates of Earth-like planets: three- dimensional climate simulations at extreme obliquity. Int J Astrobiol 2(1):1–19
- Wu CH, Lee SY, Chiang JCH, Hsu H (2016) The influence of obliquity in the early Holocene Asian summer monsoon. Geophys Res Lett 43:4524–4530
- Wu GX, Liu Y, He B, Bao Q, Duan A, Jin FF (2012) Thermal controls on the Asian summer monsoon. Sci Rep 2:404
- Wu YT (2008) Equilibria of diffusive moist static energy balance model. Progr Stud Perspect Challeng GFD 2008:348–368
- Xie SP (2004) The shape of continents, air–sea interaction, and the rising branch of the Hadley circulation. In: Diaz HF, Bradley RS (eds) The Hadley circulation: present, past, and future. Springer, New York, pp 121–152
- Xie SP, Philander SGH (1994) A coupled ocean-atmosphere model of relevance to the ITCZ in the eastern Pacific. Tellus 46A:340–350
- Yoshimori M, Broccoli AJ (2008) Equilibrium response of an atmosphere-mixed layer ocean model to different radiative forcing agents: global and zonal mean response. J Clim 17:4399–4423

Publisher's Note Springer Nature remains neutral with regard to jurisdictional claims in published maps and institutional affiliations.

